A Cells Capture, Separation and Detection Modelling Method in the Microfluidic and IDEs Based Biosensor

By

Xianglou Chen

A thesis submitted in partial fulfillment of the requirements for the degree of

Master of Science

in
Microsystems and Nanodevices

Department of Electrical and Computer Engineering
University of Alberta

Abstract

Lab-on-a-Chip technologies have been developed over the past few decades and it has a wide range of applications. For example, in the field of medicine and agriculture, portable devices with the biosensoring function have a great potential in disease detection for animals and crop disease prevention for plants. To capture the targeted cells from real and complicated biological samples, dielectrophoresis (DEP) was proposed. A DEP force could be employed as a label-free technology for achieving target cell capture and separation. Target cells can then be detected and counted using impedance spectroscopy. To prevent the targets from being drafted away during the measurements, the frequency range of DEP should overlap the impedance measurement frequency. In this study, we use a sample interdigitated electrode configuration to explore the impacts of DEP force, and also to figure out the feasible frequency range during the capture, separation, and detection of cells in the microfluidic system. Simulations provide a modelling method and guidance of a kinetics system in the microfluidic channel.

Table of Contents

Chapter 1 Introduction

1.1 Background

Nowadays, a biosensor has a wide area of applications and is a powerful analytical tool for drug discovery, medical diagnostics, food safety, agricultural and environmental monitoring, and even security and defense [1]. A popular design of the biosensor is based on the microfluidics technology and could be seen as a lab on a chip (LOC). The microfluidic technologies have been more and more required in recent for practivality [2]. Technologies are developed to process down a single lab or multiple labs to a portable chip-format device that can perform a chemical or electrical characteristic analysis. Numerous potential benefits of devices come with portable size, reduced cost, faster operation (detecting to analyzing) time, and increased accessibility to the prospective test [3-7].

A biosensor can be defined as a compact analytical device, which usually consists of two main characteristic components, recognition elements and detection elements [8-10], where recognition is the center of the molecular biosensing design [11]. Bio-recognition can be achieved by the process where the bioreceptor is combined with analytes, such as Enzymes, Cells, aptamers, DNA and other nanoparticles [14]. The accompanying might be a specific binding or non-specific binding with or without energy changing in different forms such as light, heat, pH, and mass can be seen as a bio-recognition signal [12,13].

Another characteristic component of a biosensor is the detection element, which is a physicochemical transducer that can respond to a specific binding report or a chemical reaction of recognition elements [15]. Common transducers for the bio-recognition signal are photo-diode, thermistor, pH electrode, and Quartz electrode [14]. These transducers convert the bio-recognition event into a measurable signal, which will be modified and turned into a digital signal and then be displayed on the devices.

The primary performances of a biosensor are selectivity, reproducibility,

stability, sensitivity, and linearity [14]. This thesis will mainly focus on the selectivity and sensitivity of a microfluidic and the Interdigitated electrodes (IDE) system based biosensor design. The microfluidic technology combines different sciences, such as chemistry, biochemistry, engineering, physics, micro-technology, nanotechnology, and biotechnology [16], and the IDEs system is based on electrical design. A simulation software called COMSOL Multiphysics was employed for the most part of simulation works. A microfluidic device can give a continuous flow in the micro-channel for the sensing process. This thesis design requires a continuous flow with relatively high sampling volume and sensing mechanisms from a microfluidic device such as a mechanical(syringe) pump or an electro-kinetic device. The detection/transducer technology in this thesis will be based on the impedance detection of the IDEs system that can provide simplicity and real-time detection [17,18]. Table 1 shows the comparison of other types of biosensors compared to this work:

Transducer	**Technique**	**Comparison**
Electrochemical	Amperometric[19,20]	Need redox elements to enhance the current production; time-consuming;
	Potentiometric[21,22]	Sensitive to the surrounding environment; time-consuming; sensitive to temperature
Optical	Surface plasmon resonance(SPR)[23,24]	Surface modification is one of the main challenges; bulky optical devices required
Mechanical	Cantilever[25,26]	Sensitive to temperature; bulky devices required
	Quatz crystal[27,28]	Sensitive to temperature and stress

1.2 Interdigitated electrodes (IDEs) system Overview

In this research, an impedimetric interdigitated electrodes biosensor theoretical simulation will be presented. This Interdigitated-electrodes (IDEs) system is popular since the detection method is based on measuring the changes in the impedance of the electrodes, caused by the binding of the nanoparticles near the surface of the electrodes. Additionally, this system is a non-faradaic electrical system, which does not need an electrochemical reaction on the electrode to create a detectable signal. Since a non-faradaic system does not apply any electrochemical reaction, it is a feasible design for label-free applications.

The entire system comes with two-electrode IDEs in the buffer solution that can be modeled by an equivalent circuit as a combination of resistors and capacitors. In Figure 1.2.1, the capacitor Cg is the parallel capacitance of the gap between two electrodes. Cdl capacitors are the double-layer effect equivalent capacitance when the electrical field is applied on the electrodes. When charged ions in the buffer solution are attracted to the surface of the electrodes, a separate layer of these charged ions will be formed which will act as a capacitor. Resistor R1 is the resistance of the buffer solution between the two electrodes. Therefore, the whole system is composed of three main components: the parallel gap capacitor C_g, the double-layer effect capacitor C_{dl}, and the gap resistor R_1. The parallel gap capacitor C_g is determined by the chip dimensions such as gap spacing, electrode thickness, and the dielectric property of the medium solution. The double-layer effect will be detailed in the following chapter. The resistor R_1 depends on the ionic concentrations of the buffer solution.

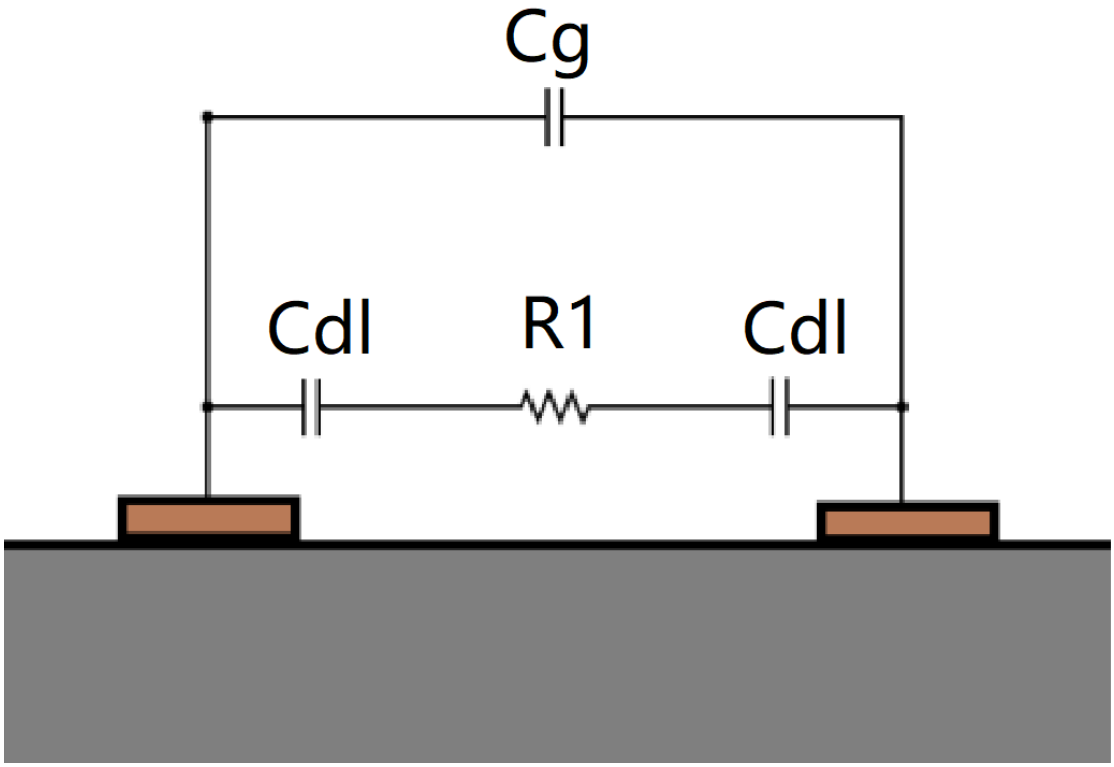

Figure 1.2.1 Equivalent circuit diagram for the two-electrode IDEs in the buffer solution, modified from [29,30,33].

As mentioned above, this system operates without any redox reactions or charge transfer to the electrodes and so it can be recognized as a non-faradaic system. Therefore, no complex circuit analysis is needed for the equivalent circuit such as charge transfer resistances or any diffusion of species in the solution that can cause a Warburg impedance on the electrodes [31,32]. This thesis will give detailed and close-to-practicality simulations of the two-electrode IDEs system's impedance to explore the differences from the ideal design.

From Figure 1.2.1, the overall impedance of the equivalent circuit can be written as [44]:

$$Z_o = (R_1 + \frac{2}{j\omega C_{dl}}) \Big\| \frac{1}{j\omega C_g} \tag{1.1}$$

Where Zo is the total impedance, ω is the angular frequency, and j is an imaginary

number. The general frequency response of the overall impedance is shown in Figure 1.2.2. In this figure, both impedance and frequency are displayed as a log scale. The impedance response has three significant regions in the frequency domain. The two cut-off frequencies from left to right are f_L and f_H, in the range from 0 Hz to the left cut-off frequency f_L; the impedance is mainly dominated by double-layer capacitors and dramatically decreases at low frequency, which will be discussed in a future chapter. The range between the two cut-off frequencies f_L and f_H is dominated by the resistance of the medium solution R1, which is why there is a flat impedance magnitude response without frequency dependence. When the frequency is higher than the right cut-off frequency f_H, the impedance magnitude decreases again, approaching 0 as the frequency increases.

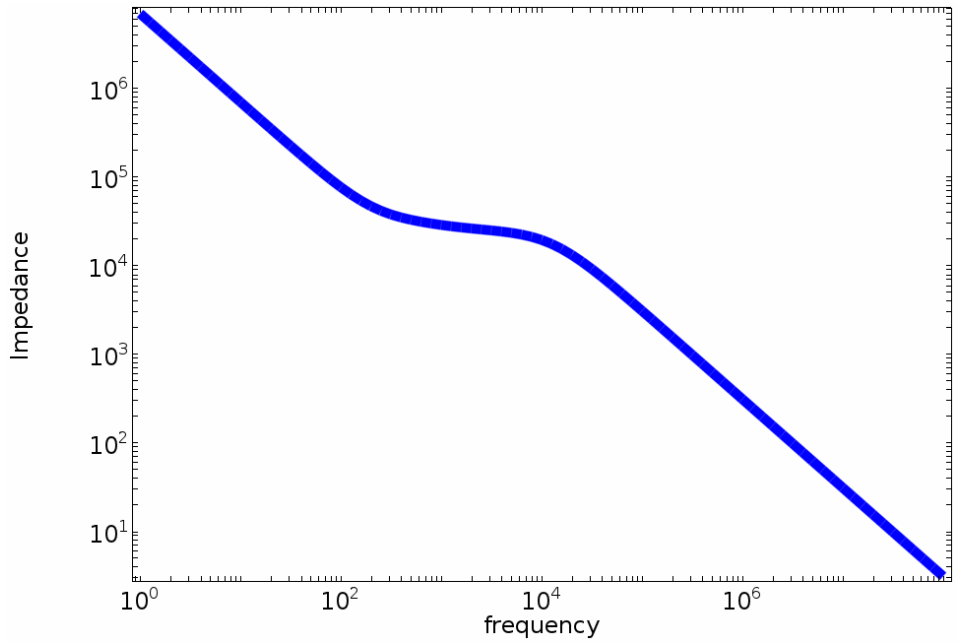

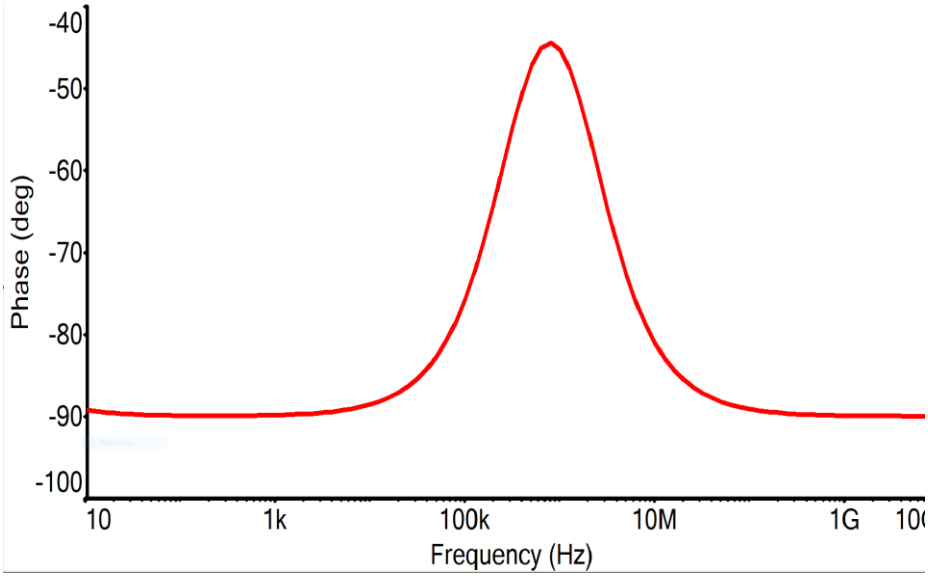

Figure 1.2.2 Impedance response with double-layer effect in the frequency domain. (a) The magnitude of impedance with two cut-off frequencies and (b) phase of impedance for the two-electrode IDEs system's equivalent circuit.

The principle of this two-electrode IDEs system is to manipulate or modify any of these parameters in the equivalent circuit to see the resulting differences in the impedance response in the frequency domain. Any captured micro-particle cells, bacteria, or bind targets could change either the conductivity between the electrodes or the dielectric properties between electrodes, depending on the properties. Thus, a measurable impedance change can be generated for detection purpose.

1.3 Micro-particles Capture

The detection method discussed in the last section has explored how the impedance response changes throughout the frequency domain. From the research work [34], applying a rotating electric field on polarizable micro-particles could move and manipulate micro-particles, such as cells or marker particles, in the liquid media. In the microfluidic system shown in Figure 1.3.1, the whole channel is filled with a homogeneous, isotropic dielectric fluid with the permittivity ε_1. When an AC voltage is applied to the electrodes, they impose a non-uniform, divergence-free electrostatic

field E_0.

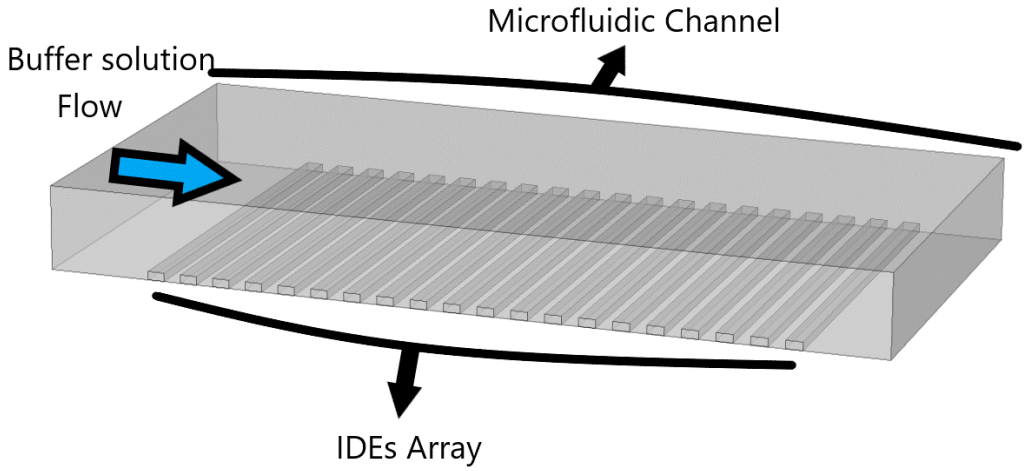

Figure 1.3.1 Simplified diagram of Microfluidic system with IDEs system.

The well-known dielectrophoresis (DEP) force is generated by the induced electrical potential when a dielectric sphere is in a dielectric medium. The expression of the DEP force is given by [35]:

$$F \equiv 2\pi R^3 \varepsilon_1 K \nabla E_0^2 \qquad (1.2)$$

In the equation (1.2), $K \equiv (\varepsilon_2 - \varepsilon_1)/(\varepsilon_2 + 2\varepsilon_1)$ is the Clausius-Mossotti (CM) factor (ε_1 and ε_2 are the complex permittivities of the medium solution and micro-particles, respectively). The sign of the CM factor will decide if the particle in the medium will be attracted to or repelled from the region of strong electric field intensity. Normally, the electric field is the strongest at the edge of electrodes. The concept and principle of the DEP force will be discussed in more detail in a future chapter.

According to the equation for the CM factor, two complex permittivities affect the DEP force. Since the complex permittivity can be given as [35], it is frequency-dependent.

$$\varepsilon_1 \to \varepsilon_1^* + \sigma_1 / j\omega \quad \text{and} \quad \varepsilon_2 \to \varepsilon_2^* + \sigma_2 / j\omega \qquad (1.3, 1.4)$$

At a specific frequency range, based on the difference between both the conductivity and relative permittivity of the micro particles, the real part of the CM factor will have a different sign as shown in Figure 1.3.2 [36]. This will lead to two different types of DEP forces (nDEP, which acts to move the particle away from the high field region, or pDEP, which acts to move the particle towards the high field region). According to the above principle, there is a feasible way to separate the different micro-particles in the microfluidic channel. This is beneficial because there are usually several different cells or particles in a red blood sample or another medical project. To find a certain frequency, one can apply a pDEP force on the aimed cells and an nDEP force on other unwanted cells to achieve the label-free cells capture process.

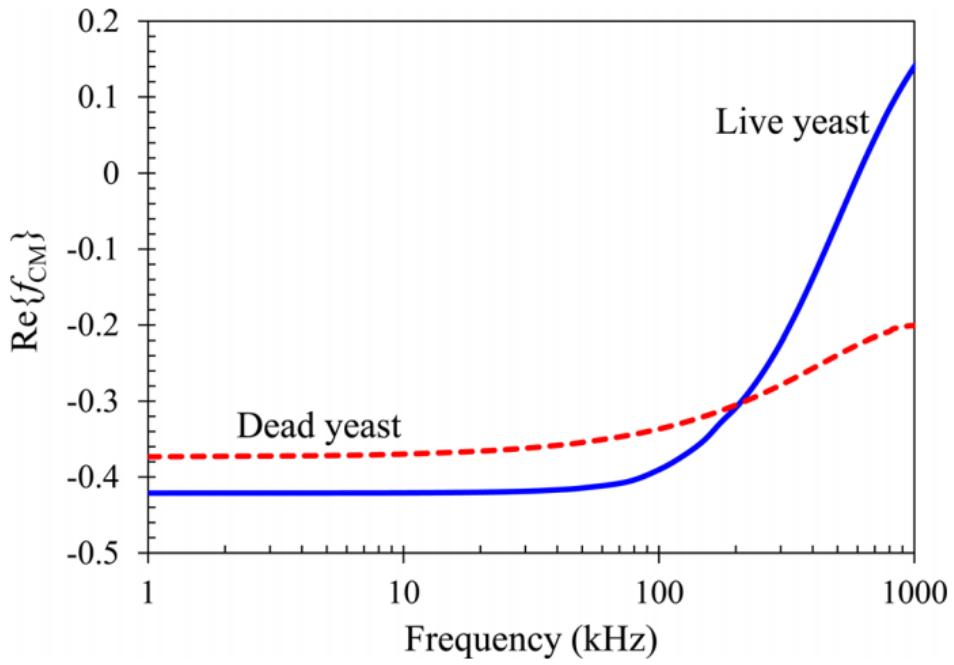

Figure 1.3.2 Comparison of the model CM factors of live (solid line) and dead (dashed line) Yeast cells suspended in 1mM phosphate buffer [36].

The CM factor simulation involves Multi-layer models that are based on the reality of the different cell's geometric structures. The Multi-layer model employs the specific permittivity and conductivity for each layer, as in the yeast cell multi-layer model shown below:

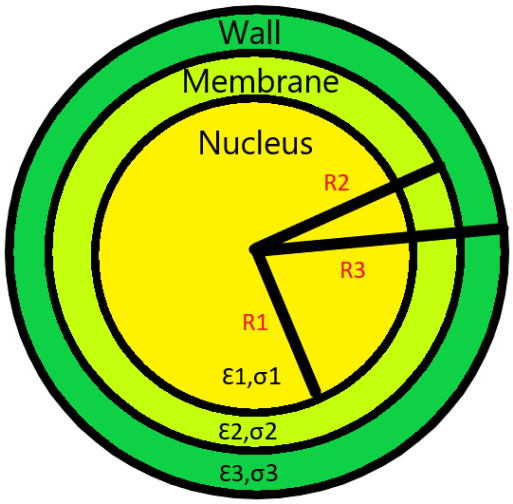

Figure 1.3.3 Physiologic diagram of multi-layer model, modified from work [36].

These close-to-reality models and simulation approaches are used to figure out the required frequency of the DEP force that can capture the target cell and repel other micro-particles by the CM factor character curve.

1.4 Goal

The primary goal of this thesis research is to simulate a label-free, portable, precise biosensor platform for recognizing, detecting, and capturing target micro-particles. Specifically, this thesis will start by proving the concepts of the IDEs system, impedance detection, and DEP force. Then, it will cover simulation including the IDEs system's electrical stationary analysis and impedance response. The target capture cell in this thesis was set up as the HEK_293 cell. Finally, the capture and separate condition for the IDEs system design and detection frequency will be figured out by simulations in COMSOL and Matlab. The target cell would be separated from other micro-particles in the microfluidic channel and will be captured by electrodes. The detection frequency range, which overlaps with the capture and separate frequency, would be found. Other factors affecting the capture and separation process on the target cell such as the flow rate in the micro-channel, an applied voltage of IDEs system, the conductivity of the medium solution, and the particle size would also be explored. The conclusion of the effect of these factors will help in coming up

with a referential value in the future chip design.

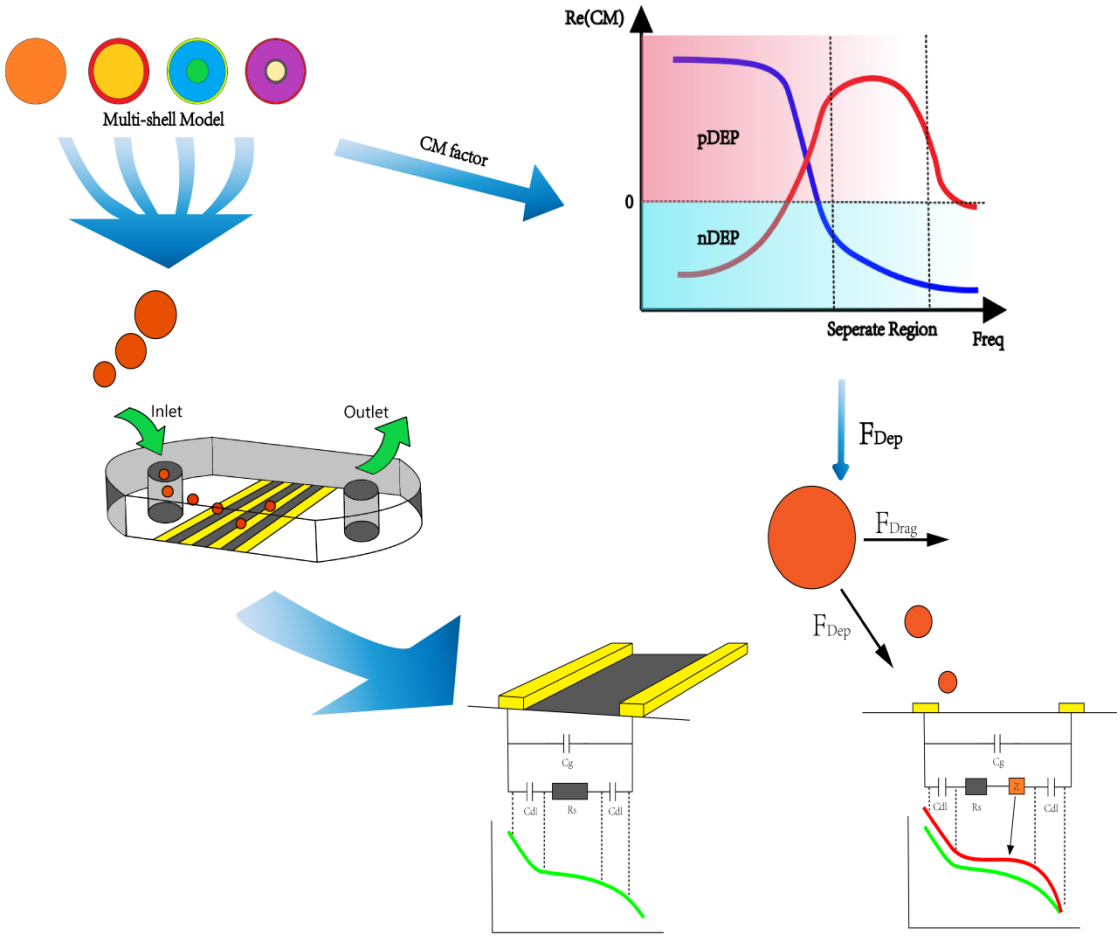

Figure 1 Principle of cell capture and detection during IDEs based biosensor

Figure 1.4.1 Overview diagram of the thesis goal.

1.5 Thesis Outline

This thesis will start with the design and proof concept of an IDEs system with early simulation results for different types of materials employed in the biosensor system in Chapter 2. The electrode gap spacing and the double-layer effect regarding the simulation will be discussed. In Chapter 3, different models for several common species of the cell will be developed, accompanied by simulation results and explanations. Chapter 4 will delve into the micro-particle capture process based on the concept of the DEP force and the principle of the microfluidic system. In Chapter 5, the ongoing and future work will be discussed.

Chapter 2 Interdigitated Electrodes (IDEs) System

2.1 Introduction

To design an IDEs system, the most important considerations are the materials, dimensions, structure of the interdigitated electrodes, and connection with the microchannel. Throughout the previous designs [37-46], the interdigitated electrodes system has been an effective method to detect bio-particles. The material of IDEs should provide high sensitivity and should not be too expensive to fabricate for practical purposes. To have sufficient sensitivity, it is required to achieve the detection process during a low concentration of bio-particles. For industrial, agriculture, and medical purposes, the metal of interdigitated electrodes should be inexpensive for use as a Point-of-Care (POC) biosensor. Different kinds of materials could be employed for insulating substrates such as plastic, glass and silicon dioxide (SiO_2). Gold and aluminum are the most popular materials that have been used for electrode nano-fabrication because of their biocompatibility and yield [47]. The dimension of the IDEs design including the digit's width, the gap spacing between the digit, and the ratio of the digit's width to the spacing are decisive to get a higher sensitivity to bind the bio-particles [48]. Because of the thesis' emphasis, the microchannel fabrication and the chip fabrication will not be included in this thesis.

2.2 Proof of Concept

A 2D model is set up for the IDEs System simulation since 2D models are easier to modify and can be solved much faster. Moreover, modeling mistakes are more easily found when working on 2D models. A simplification of a 2D model is represented in Figure 2.2.1.

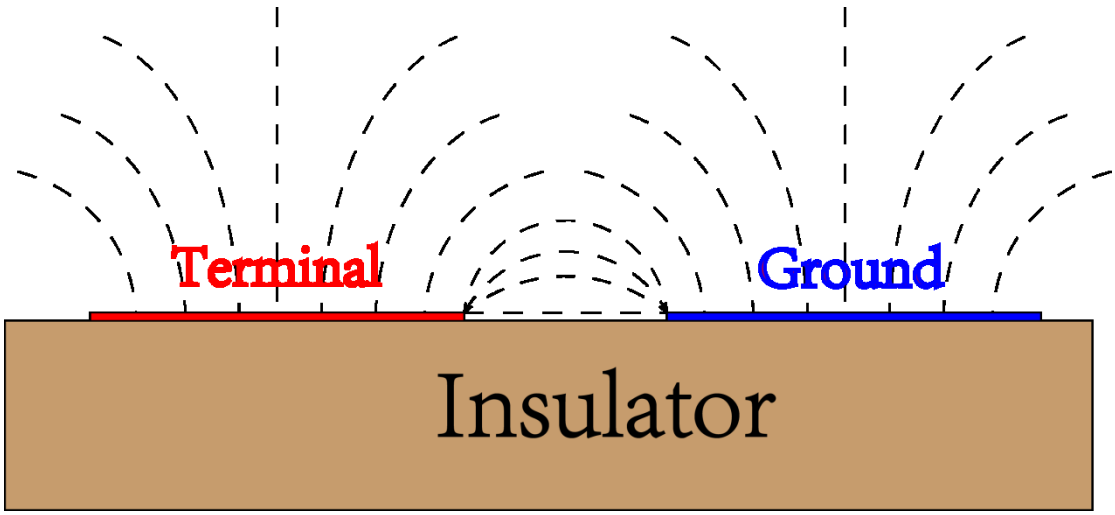

Figure 2.2.1 A simplified representative model of the 2D IDEs system model showing a pair of electrodes finger.

The capacitance between two electrodes gap can be calculated by:

$$C = \frac{Q}{U_0} \tag{2.1}$$

Where the micro-particle in the electrical field supported by the IDEs system can change the charge density on the surface of electrodes according to the Gauss' Law.

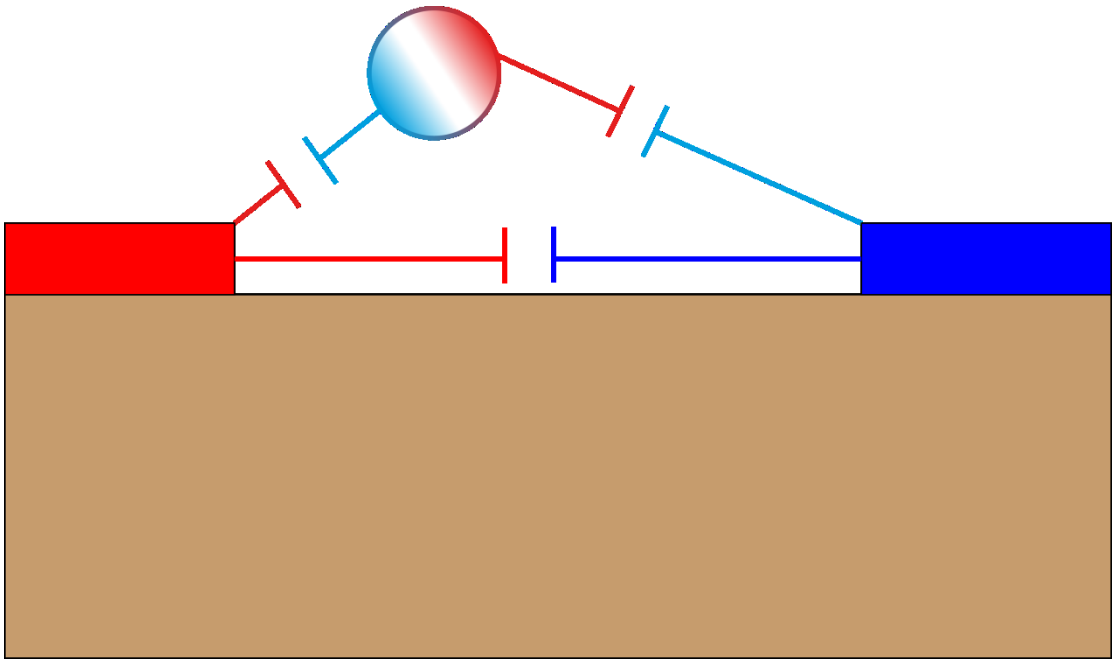

Figure 2.2.2. Schematic of capacitance between electrodes and a metal particle.

When an aluminum particle was approaching the electrodes, the distance between the particle and electrodes decreased. According to $C = \varepsilon \frac{A}{d}$, a parallel capacitor to each electrode side becomes more significant in this system as is shown in Figure 2.2.2. The charge density and charge distribution on the electrode surface was also affected when the particle invaded. Figure 2.2.3 shows the simulation results of an aluminum particle approaching the electrode surface, with the space charge density in a 2D color plot. Table 2.1 records the surface charge density of the electrodes.

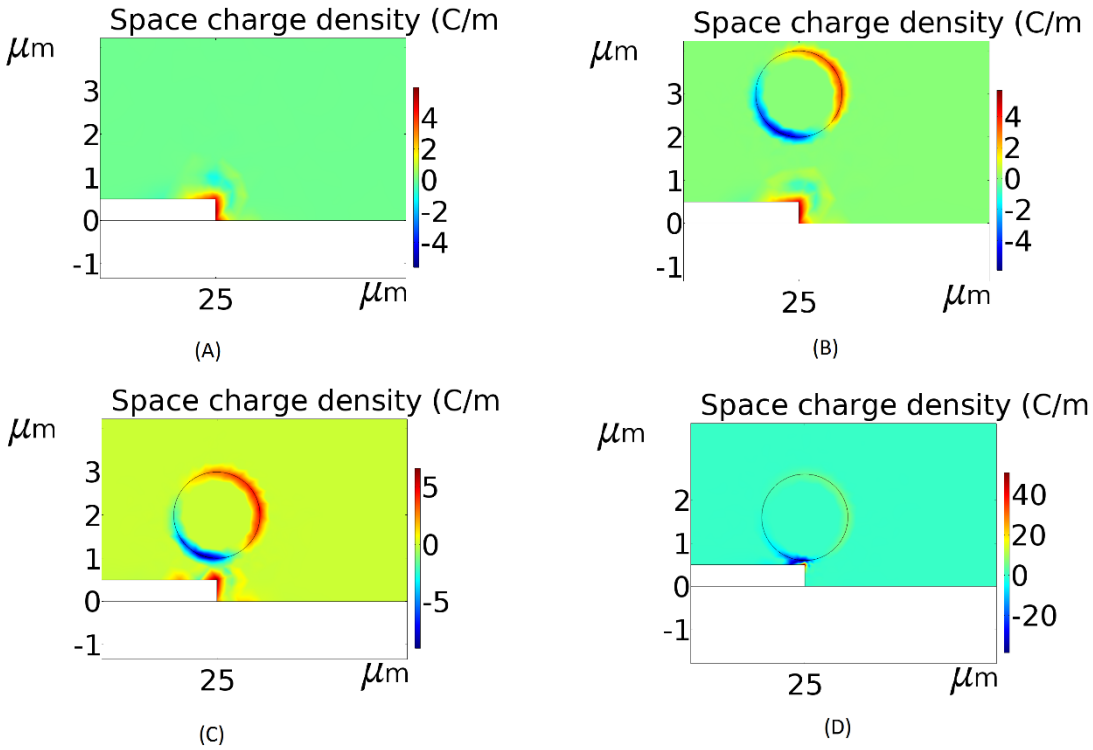

Figure 2.2.2 The space charge density changing due to the micro-particle.

Figure 2.2.2 shows (A) charge density of an aluminum electrode surface, (B) space charge density of an aluminum electrode surface when a gold micro-particle is 1.5 micrometers above the electrode surface, (C) space charge density of an aluminum electrode surface when an aluminum micro-particle is 0.5 micrometers above the electrode surface, and (D) space charge density of an aluminum electrode surface when an aluminum micro-particle is touching the electrode surface.

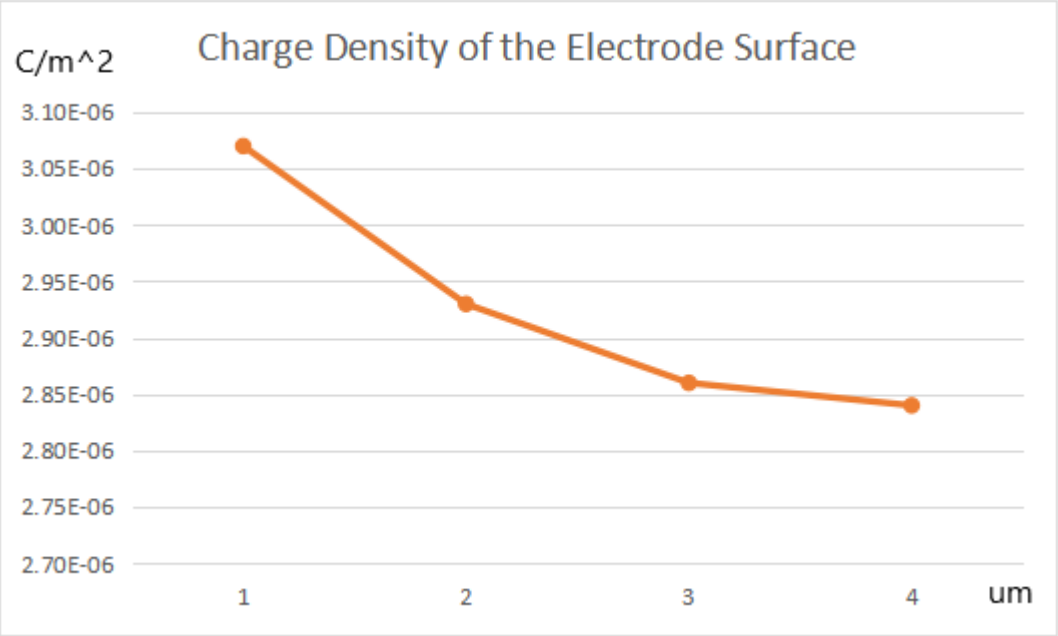

Table 2.1 The surface charge density of the electrodes when an aluminum micro-particle is approaching the electrode surface. (X-axis indicates the distance from the center of the micro-particle to the electrode surface. Y-axis indicates the charge density of the electrode surface.)

For detection, these changes in the surface charge density will affect the capacitance of the electrodes. When the micro-particle was closer to the electrode surface, the charge density on the electrode increased as shown in Table 2.1. According to equation 2.1, this charge increment was caused by the increase in capacitance. Where impedance is given by $Z \propto \frac{1}{C}$, the impedance will decrease according to this increment of the capacitance in the system. The slight impedance changes can be theoretically seen as a detection signal and are captured by the measurement circuit. Therefore, for the certain target particle to generate a significant change in the impedance variation, it is important for the design to obtain a high sensitivity of the biosensor.

2.3 Double-layer Effect

In a biological system that has particularly high conductivity, there is an increasing need to consider and understand the dynamics and kinetics of processes in a wide range of frequencies [49-54]. Although dielectric spectroscopy (DS) and impedance spectroscopy (IS) can be strong methods for the investigation of biological samples, these measurement techniques are disturbed by a contemporary influence when a voltage is applied on a highly conductive biological system [55]. It is because, when an electric field is applied, the dissolved free ions wander freely and tend to move towards the electrode thus developing an ionic double-layer. This double-layer region is shown in Figure 2.3.1 [55] and will induce a huge electrical polarization of the material and a "near-absence" of the electric field at low frequencies [49,50].

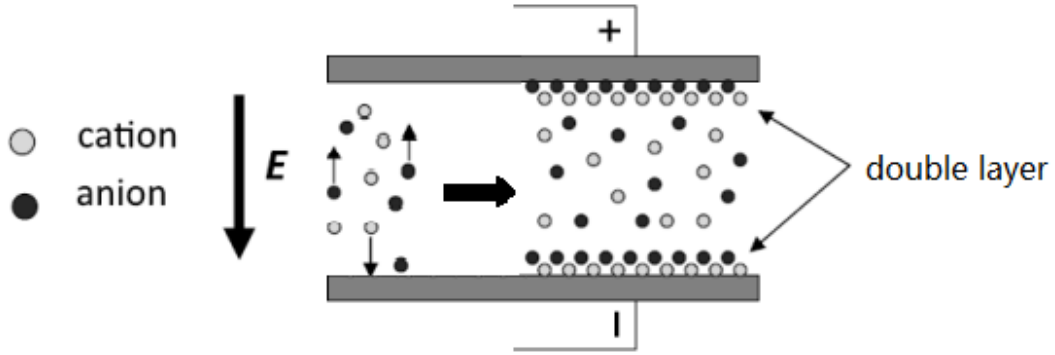

Figure 2.3.1 The modified schematic of the double-layers region produced by an applied electrical field [55].

The polarization electrical field Ep and bulk electrical field Eb were imposed by electrical field E, where $E = Eb + 2Ep$ and 2Ep >> Eb. These layers can be thought of as a resultant capacitance that will dominate the signal at lower frequencies [55]. The resultant capacitance leads to a difficulty in the interpretation of the data, where the measured characteristic is far from the real character of the material.

To get a more realistic model for the impedance simulation in this thesis, the double-layer effect on the electrode was considered and modeled. A new layer was established around each electrode and the thickness of the layer could be found by the

Debye length equation [56]:

$$\lambda_D = \sqrt{\frac{\varepsilon k_B T}{2 n_0 e^2}} \tag{2.2}$$

where Ɛ is the dielectric constant of the medium, k_B is the Boltzmann constant, T is the temperature, n_0 is the concentration of the ions, and e is the elementary charge.

This calculation is verified with a concentration based "Transport of Diluted Species" module COMSOL simulation, which is implemented to visualize the double-layer as shown in the 2D model below:

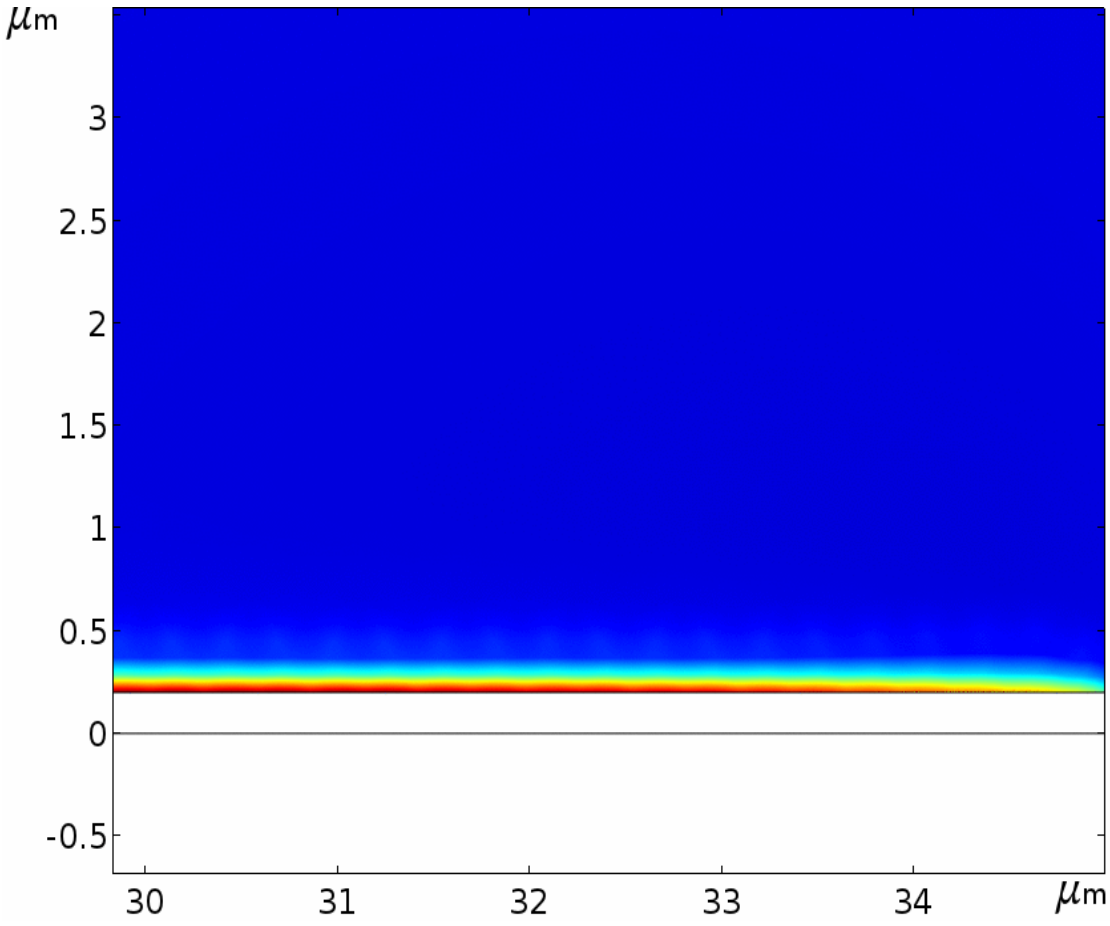

Figure 2.3.2 COMSOL simulation model of Double-layer (reddish film area) on the electrode.

The dielectric constant of this layer should be defined as the Helmholtz model [57]

which is a simpler model that could lead to a capacitance (per unit area):

$$C_H = \frac{\varepsilon}{H} \tag{2.3}$$

where Ɛ is the dielectric constant and H is the radius of the ions. This model is expanded to the Gouy model [58] and the Chapman model [59] by adding Maxwell-Boltzmann's statistics that account for the distribution of diffused ions. The model, therefore, can be adjusted to [58,59]:

$$C_{GC} = \frac{\varepsilon}{\lambda_D} \cosh \frac{e\Phi}{k_B T} \tag{2.4}$$

Where ϕ is the electric potential, e is the elementary charge, kB is the Boltzmann constant, T is the temperature in Kelvin, and the Debye length $\lambda_D = \sqrt{\frac{\varepsilon k_B T}{2 n_0 e^2}}$.

The two models can be combined by treating the Helmholtz model's and the Gooey-Chapman model's capacitance as capacitors in series [60], resulting in a complex model called the Stern model. Overall, the region around the electrode can be considered to be consisting of one stationary Helmholtz layer and another diffused layer of ions as defined in the Gouy-Chapman model. The capacitance per unit could be expressed after the combination [60]:

$$\frac{1}{C_S} = \frac{1}{C_H} + \frac{1}{C_{GC}} \tag{2.5}$$

For a practical situation, such as in the medical industry, the concentration of the buffer ion will be restricted to a relatively low value [61]. At a low ion concentration, the Gouy-Chapman capacitance C_{GC} in the equation (2.5) will be much greater than the Helmholtz capacitance C_H. In this case, it can be estimated as $\frac{1}{C_S} = \frac{1}{C_{GC}}$ where

the equation of the Gouy-Chapman model can also be simplified as [58,59,60]:

$$C_{GC} = \frac{\varepsilon}{4\pi\lambda_D}\cosh(\frac{\phi_0}{2})\frac{\sqrt{2}\,|\sinh\frac{\phi_0}{2}|}{\cosh\phi_0\sqrt{\ln(\cosh\phi_0)}} \tag{2.6}$$

In the equation (2.6), $\Phi_0 = \frac{e\Phi}{k_B T}$ and the Debye length can be calculated using equation 2.2 and can be verified as the thickness of the double-layer simulated in the model as shown in Figure 2.3.2. As indicated in the equation (2.3), the dielectric constant of double-layer is given by $\varepsilon_{DL} = C^*\lambda_D$. The impedance model was discussed in Chapter 1, and the equivalent circuit was shown in Figure 1.2.1. The overall impedance can be expressed as:

$$Z_o = (R_1 + \frac{2}{j\omega C_{dl}}) \Big\| \frac{1}{j\omega C_g} \tag{2.7}$$

The simulations were done in COMSOL 5.4a and the results are shown in Figure 2.3.3:

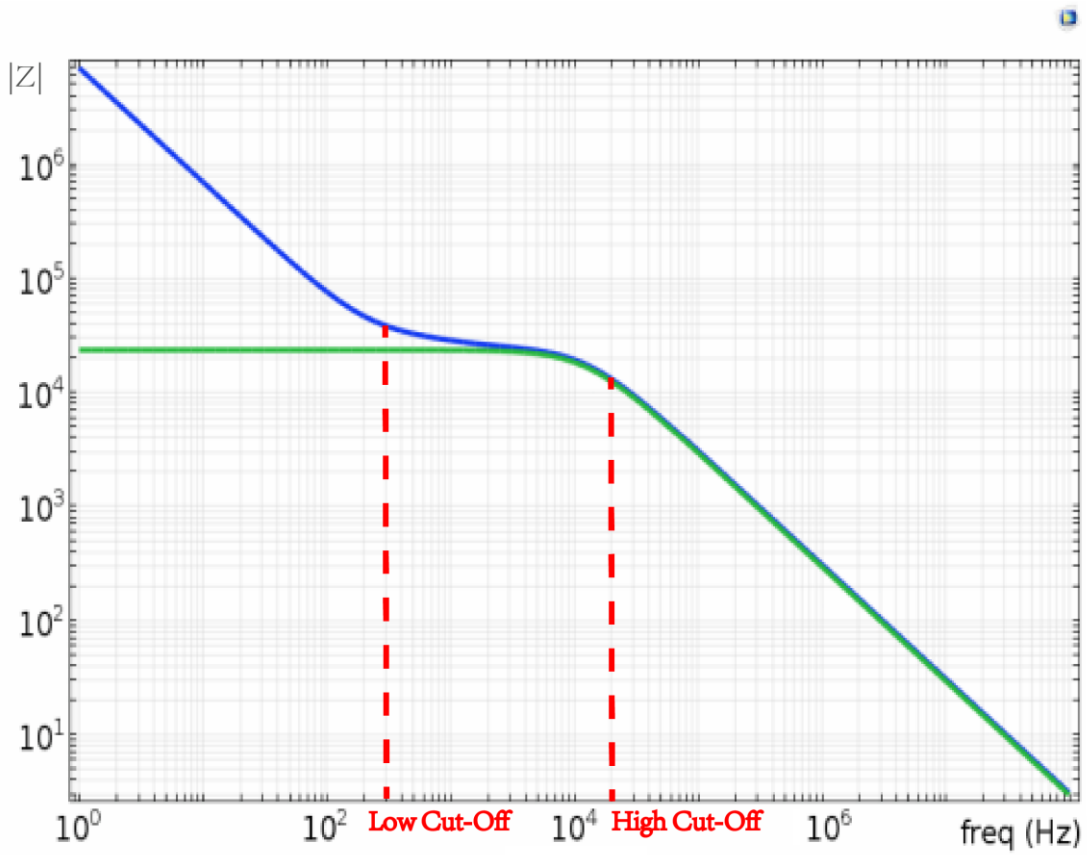

Figure 2.3.3 The impedance magnitude responses of the IDEs system 1) The green line shows the impedance response of the IDEs system without the double-layer effect. 2) The blue line shows the impedance response of the IDEs system with the double-layer effect.

Figure 2.3.3 shows the significant differences at a lower frequency, where the double-layer capacitance dominates the impedance response; the impedance dramatically decreases from a high level at low frequency. When the frequency increases to the "Low cut-off" frequency, the impedance response will be dominated by the resistance of the medium solution. As the frequency increases to the "High Cut-off" frequency, the impedance response will be dominated by the gap parallel capacitor, and then it decreases again. Since the parallel metal gap capacitor dominates the region after the "High Cut-off frequency" defined by [62] $F_{H-cutoff} = \frac{1}{2\pi R_1 C_g}$ impedance magnitude decline close to 0.

2.4 Material of the IDEs system

One of the most popular materials for making biocompatible electrodes is gold, which does not oxidize or corrode easily [63-65]. Glass was widely used during the common substrate's fabrication, but it can be difficult to pattern metals on glass. However, silicon dioxide grown on a silicon wafer can be a suitable alternative [66]. For practical fabrication considerations, aluminum can replace the gold electrodes because it is cheaper and has a higher yield [66].

The simulation results for impedance magnitude and the phase response of both materials are shown in Figure 2.4.1.

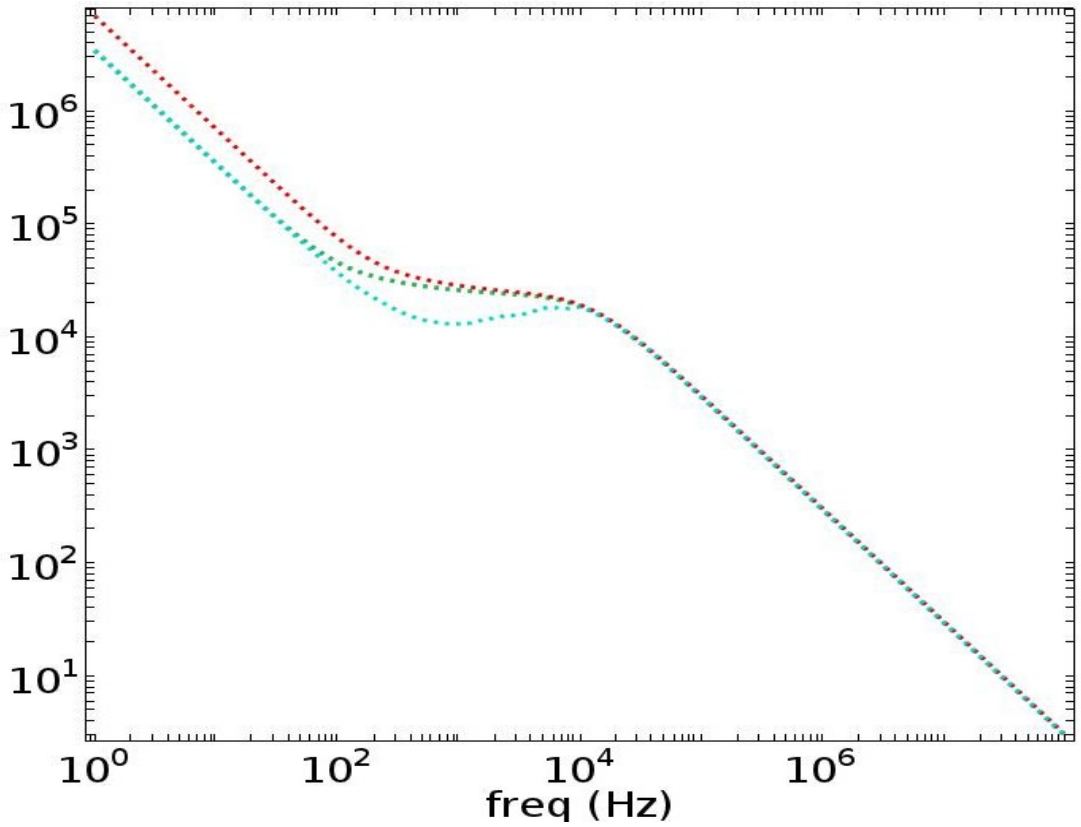

Figure 2.4.1 COMSOL simulation results of Impedance responses of gold and aluminum electrodes.

In Figure 2.4.1, the red line shows the impedance responses in the magnitude of gold electrodes and the green line shows the impedance responses in the magnitude of aluminum electrodes. The mint/blue line shows the magnitude of the impedance response when the micro-particle was dropped in the center of the electrode gap. The sensitivity of the IDEs system mainly depends on the difference of the electrode's impedance responses before and after the micro-particle dropped in. According to Figure 2.4.1, the impedance magnitude and phase response of gold and aluminum are slightly different in the resistor region where the particle has a significant effect on the impedance response. Thus, considering the commercial and industrial purposes, aluminum is a better choice for replacing gold as the electrode material, which can also be also by the phase response of impedance shown in Figure 2.4.2.

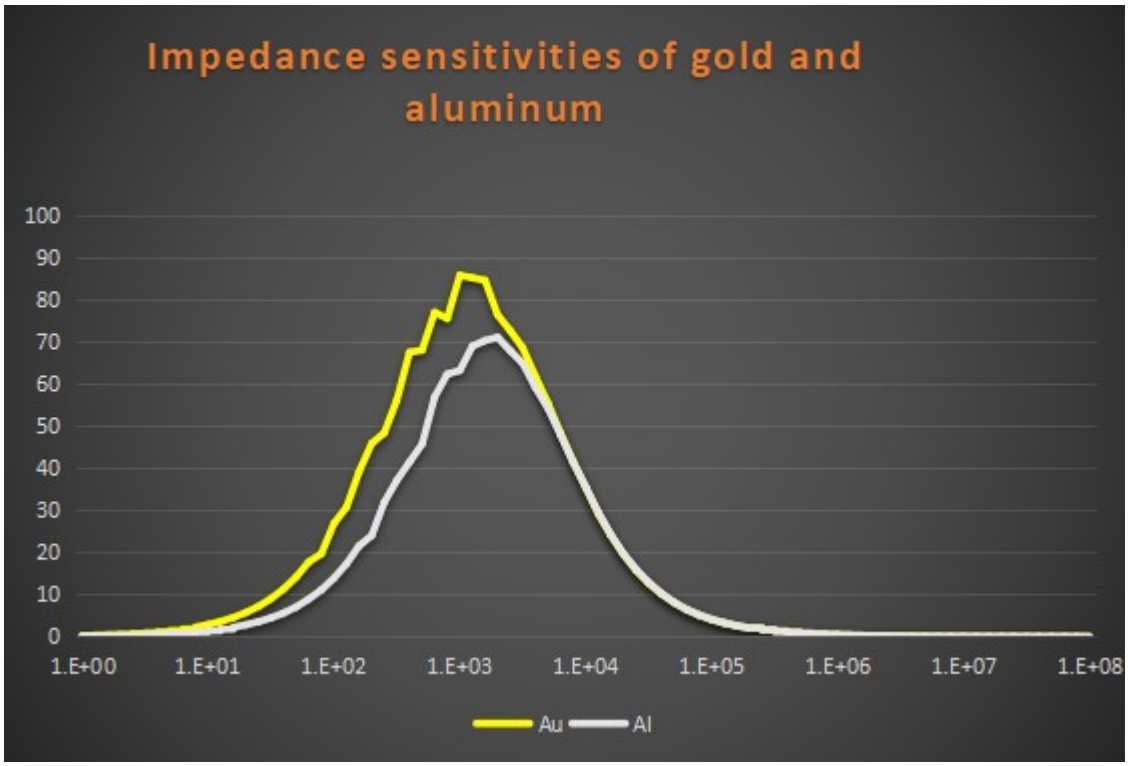

Figure 2.4.2 Impedance sensitivities of gold and aluminum electrodes. 1) The gold line is the sensitivity of the gold electrode. 2) The silver one is the sensitivity of the aluminum electrode.

2.5 Dimensions of electrodes and gap spacing

Another important factor of sensitivity is the dimension of the IDEs system. The target micro-particle of this thesis design will be plastic beads, Yeast cells CHO_7, and HEK 293 cells. The radius of these micro-particles ranges from 4 micrometers to 12 micrometers, therefore, the gap spacing was set up as 10 micrometers for the purpose of capture. The ratio of the electrode to the gap spacing can have a significant effect on the impedance responses. To counter this, a series of simulations were followed at a range of frequencies and different electrode width to gap spacing ratio ranging from 1:2 to 8:1, and aluminum was selected as the material of the electrodes. The simulation results are shown in Figure 2.5.1:

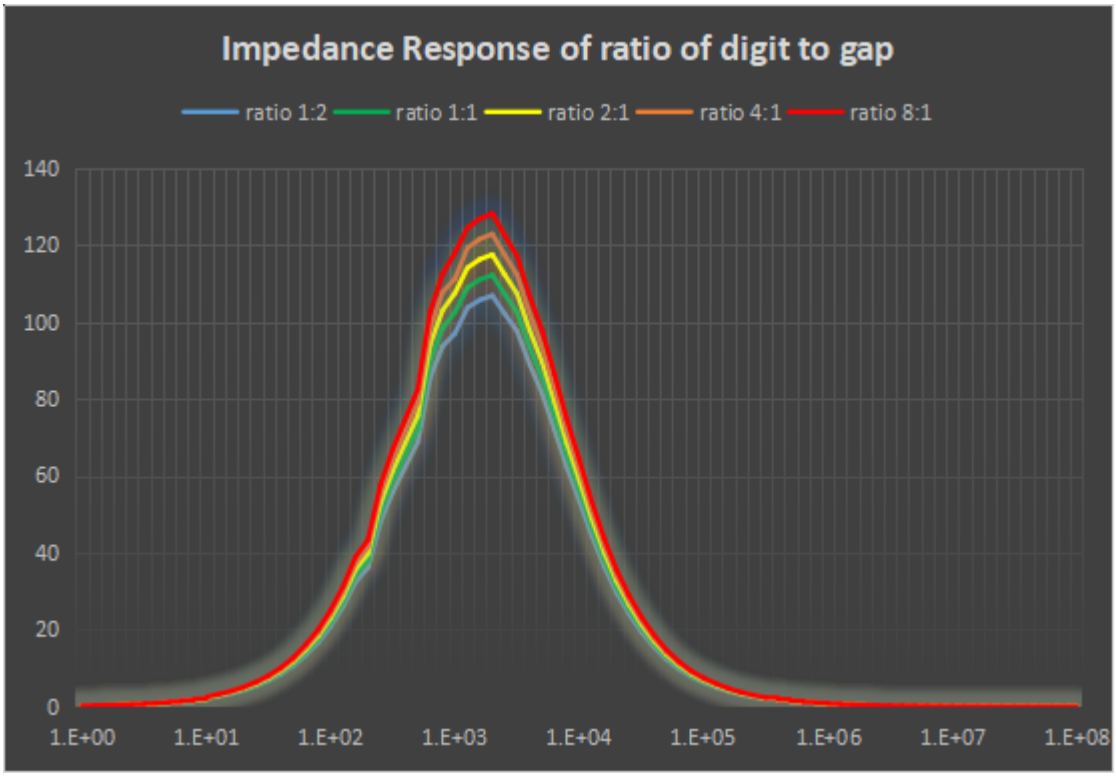

Figure 2.5.1 The impedance responses of various ratios of electrode width to gap spacing.

According to the simulation results shown in Figure 2.5.1, when the ration was increased, the impedance response also increased slightly. With the practical cost and fabrication constraints, the ideal electrode dimensions would minimize the digit width and even reduce the gap size. To ensure the electrodes are affordably and reliably fabricated, this thesis will use the ratio 2:1 as the electrode dimension.

2.6 Distribution/Position of Micro-particle

In reality, the position of micro-particles around the electrodes can affect the impedance response during the detection and capture process. These micro-particles are captured by electrodes around the edge of the electrode by employing the DEP force. The impedance responses could be affected by the different positions of the micro-particles. Thus, simulations are based on the position of micro-particles around the electrode edge. Figure 2.6.1 shows the simulation results of the impedance responses of different positions of the micro-particles.

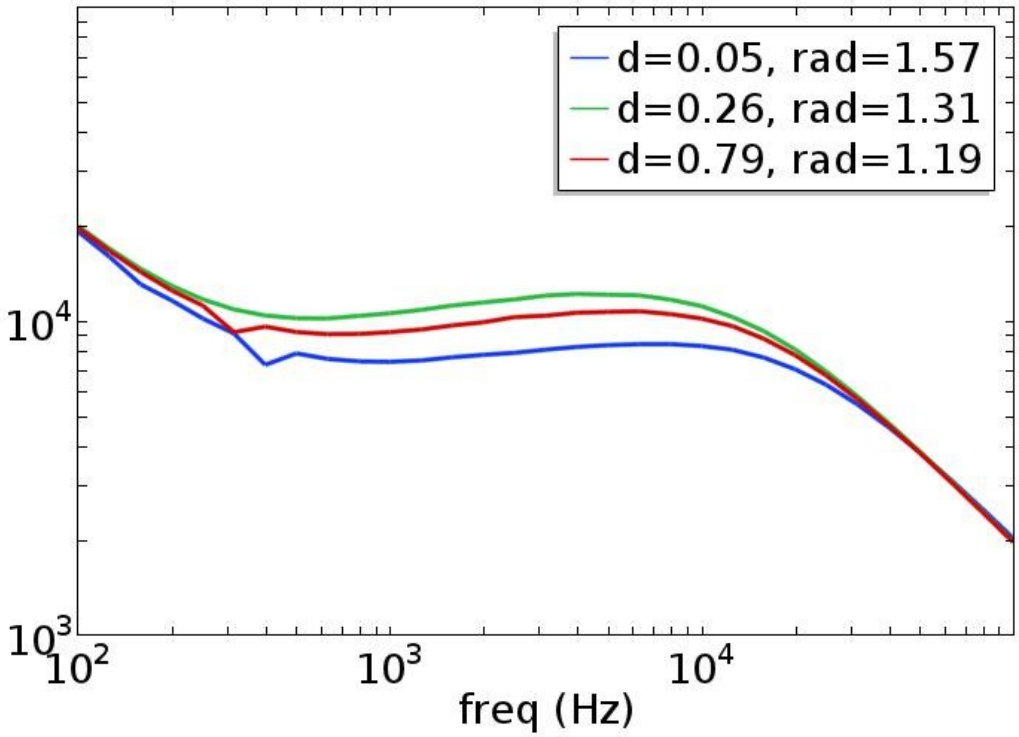

Figure 2.6.1 Impedance responses of different positions of the micro-particles.

In the figure, we can see the three different positions of micro-particles spinning around the electrode vertex. The positions were selected based on the geometry of the electrode, the double-layer and the distance to the particle normal. The angle between the horizontal direction and the electrode vertex to the particle center point was recorded and is shown in the legend of Figure 2.6.1. Compared to the impedance response shown in figure 2.4.1, the position of the captured particle did an interference on the impedance response, but it was under the tolerance of the detection system. The number of the captured particle also has a significant effect on the IDEs system. However, based on the 2D model, it is not under consideration, which will be in future work. It can also be avoided by utilizing the microwell process to give a physical restriction to obtain a single cell capture.

2.7 Conclusion

This chapter had a detailed discussion on the IDEs system's principle and concepts. Abundant simulation models were set up in COMSOL to explore as many factors as possible for the characteristic of the IDEs system. As the basic structure of the biosensor, the IDEs system should be sensitive enough for the detection of

micro-particles. The material of the biosensor should be affordable and reliable for commercial and industrial purposes; therefore, aluminum was selected as the electrode material. Additionally, to save the cost of fabrication and power consumption, the dimension of the electrode to the gap space ratio was set up as 2:1. This provides a sufficient impedance response for detection, which is good for a PoC or a portable device in terms of cost and power supply. Finally, this chapter discussed the impedance responses for a close-to-reality situation, which will be further discussed in the following chapter with the DEP force capture process.

Chapter 3 Dielectrophoresis (DEP) force

3.1 Introduction

Dielectrophoresis (DEP), which can occur when a dielectric particle is placed in a non-uniform electrical field, is an ideal method to control the electrically neutral particles [67]. There are two types of DEP forces based on the study of the CM (Clausius-Mossotti) factor. If the DEP force compels a micro-particle to move towards a high gradient region of the electric field, the type of DEP force is positive (pDEP). If the DEP force compels a micro-particle to move away from a high gradient region of the electric field, it is a negative DEP (nDEP).

The magnitude of the DEP force is dependent on the dielectric properties of the micro-particles and the suspension media. When a micro-particle is immersed in a suspension medium, the polarizability of the micro-particle will contribute significantly to the DEP force [68]. In this chapter, the concept and principle of the dielectrophoresis force will be discussed at first. Models with multiple shells and layers, employed in both the capture process and detection simulation, would be introduced. To achieve the capture process and the separate process goal of the biosensor design, the DEP force will be utilized and generated in the IDEs system.

3.2 Proof of Concept

A homogeneous spherical particle can be seen as a theoretical model for DEP when the particle is immersed in a dielectric medium. For a homogeneous spherical particle of radius R in a medium with permittivity ε_m, the DEP force of this model can be calculated as follows:

$$F_{DEP} = 2\pi r^3 \varepsilon_m \mathrm{Re}(f_{CM}) \nabla |E|^2 \tag{3.1}$$

where f_{CM} is the Clausius-Mossotti (CM) factor, r is the radius of the particle and ε_m^* is the permittivity of the medium. The equation (3.1) can be adjusted to equation (3.2) for a non-spherical shaped particle [69]:

$$F_{DEP} = \frac{\pi r^2 l}{3} \varepsilon_m \mathrm{Re}(f_{cm}) \nabla |E|^2 \tag{3.2}$$

where r is the radius and l is the length of an ellipsoid particle. This equation is usually used to model the dielectrophoretic response of red blood cells and carbon nanotubes [68].

According to equation (3.1) and equation (3.2), if a certain IDEs system was given a certain micro-particle, the direction or the type of the DEP force will depend on the real part of the CM factor. The CM factor included in equation (3.1) and equation (3.2) is defined by complex permittivity (dielectric constants) as:

$$f_{CM} = (\varepsilon_p^* - \varepsilon_m^*)/(\varepsilon_p^* + 2\varepsilon_m^*) \tag{3.3}$$

ε_p^* and ε_m^* express the complex permittivity of the particle and medium respectively, and can be calculated by the relative permittivity ε_p and conductivity σ_p.

$$\varepsilon_p^* = \varepsilon_p - i(\sigma_p / \omega) \tag{3.4}$$

Here, i is the imaginary unit and ω is the angular frequency. The complex permittivity of the medium takes the same equation form, thus, the CM factor is a frequency-dependent parameter for a certain particle and medium. The sign of the real

part of the CM factor can cause a difference in direction of the DEP force. The real part of the CM factor depends on the frequency.

As mentioned before, the sign of the CM factor will directly determine the type of the DEP force (nDEP or pDEP). A positive CM factor occurs when the particle's polarizability is greater than the medium's polarizability and is defined as [70]:

$$P = 3\varepsilon_0\varepsilon_m\left(\frac{\varepsilon_p - \varepsilon_m}{\varepsilon_p + 2\varepsilon_m}\right)E_0 \tag{3.5}$$

The field inside the sphere is given by $E_i = -\nabla\phi_i = \frac{3\varepsilon_m}{\varepsilon_p + 2\varepsilon_m}E_0$, so the polarization P can be expressed as [70]:

$$P = (\varepsilon_p - \varepsilon_m)\varepsilon_0 E_i \tag{3.6}$$

According to equation (3.5) and equation (3.6), it is very important to select the right medium to suspend particles to get the expected polarizability. The DEP force will change with the relative polarizability when the particle has greater polarizability or lesser polarizability than the medium; the particle will move along the direction of the DEP force. When the real part of the CM factor is positive, leading to pDEP, the particle will move towards to the higher electric field region. On the contrary, when the particle experiences an nDEP, it will move away from a high electric field region to a low electric field region. The directions of the motion of a particle in pDEP and nDEP are shown in figure 3.2.1.

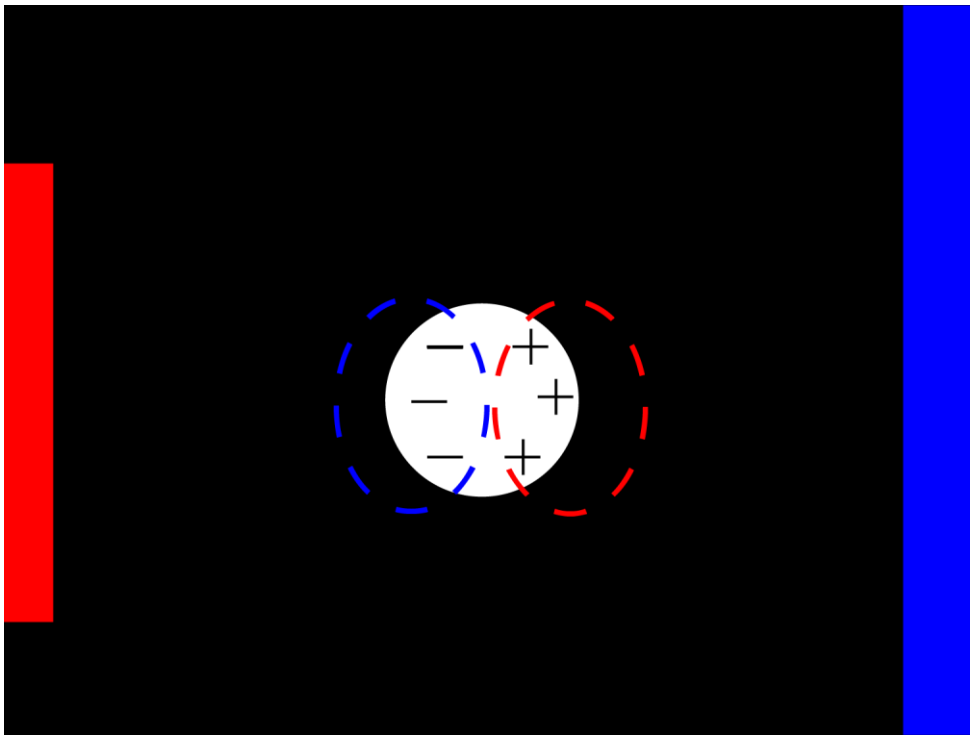

Figure 3.2.2 Particle movement tendency during pDEP in a non-uniform electrical field.

In addition to plastic beads, more varieties of micro-particles will be included such as Yeast cells and HEK 293 cells for further research. Regarding the structure of these three kinds of micro-particles, a plastic bead is the simplest—it is a solid，homogeneous, and zero-shell sphere. For a zero-shell model, the complex permittivity of the particle and medium can be defined by [71,72]:

$$\varepsilon_p^* = \varepsilon_p - i\sigma_p / \omega \tag{3.7}$$

$$\varepsilon_m^* = \varepsilon_m - i\sigma_m / \omega \tag{3.8}$$

The complex permittivity is more complicated for a biological particle model because of the more complex heterogeneous structure that contains more than one layer. For biological particles such as Yeast cells and HEK 293 cells, the complex internal structures such as the cell wall, membranes, cytoplasm, and cell nucleus have different permittivities and conductivities. Therefore, different multiple-layer models are set up for these biological particles based on the different internal dielectric

properties.

3.3 Multiple Layer Models

To get close-to-reality simulation results, the refining method has applied different multiple layer models on the four target particles in this thesis work. Those models would be employed in three main simulations among the detection, capture, and separation process in order to help figure out the frequency range, flow rate, and apply voltage for the system design. Models are designed with regards to the biological structures and are developed from a single-layer model. For a single-layer model, the overall dielectric property is obtained from a combination of the properties of the outer shell and the inner core [73,74]:

$$\varepsilon_p^*(\omega) = \varepsilon_m^* \frac{\left(\frac{R}{r}\right)^3 + 2\frac{\varepsilon_o^* - \varepsilon_i^*}{\varepsilon_0^* + 2\varepsilon_i^*}}{\left(\frac{R}{r}\right)^3 - \frac{\varepsilon_0^* - \varepsilon_i^*}{\varepsilon_0^* + 2\varepsilon_i^*}} \tag{3.9}$$

Where the permittivities are the complex permittivities of the particle's outer shell and inner membrane that can be calculated by using equation (3.7) or (3.8). Term r (which is equal to R-d, d is the thickness of the outer layer) is the inner radius and R is the outer radius. This model can be visually indicated as shown in Figure 3.3.1:

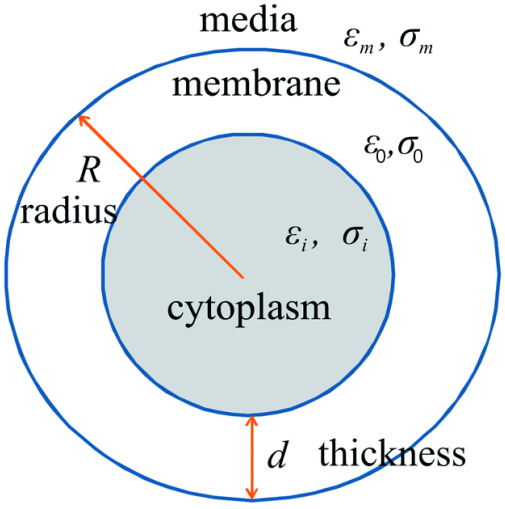

Figure 3.3.1 Single-shell model of HEK 293 cell considering different dielectric

properties for the cytoplasm and membrane, modified from [73].

Another single-shell dielectric model could be expressed by equation (3.10) [75], in terms of cytoplasm conductivity σ_c, permittivity ε_c, membrane capacitance C_m, and membrane conductance G_m.

$$\varepsilon_p^* = \frac{(C_m + \frac{G_m}{j*\omega})r \times (\varepsilon_0\varepsilon_c + \frac{\sigma_c}{j\omega})}{(C_m + \frac{G_m}{j\omega})r + (\varepsilon_0\varepsilon_c + \frac{\sigma_c}{j*\omega})} \tag{3.10}$$

Based on the single-layer model, this can be developed into a multiple-layer model by equation 3.11. The complex permittivity can be computed as follows [70]:

$$\varepsilon_c^* = \varepsilon_1^* \frac{\left(\frac{r_1}{r_2}\right)^3 + 2\left(\frac{\varepsilon_{23}^* - \varepsilon_1^*}{\varepsilon_{23}^* + 2\varepsilon_1^*}\right)}{\left(\frac{r_1}{r_2}\right)^3 - \left(\frac{\varepsilon_{23}^* - \varepsilon_1^*}{\varepsilon_{23}^* + 2\varepsilon_1^*}\right)} \tag{3.11}$$

And

$$\varepsilon_{23}^* = \varepsilon_2^* \frac{\left(\frac{r_2}{r_3}\right)^3 + 2\left(\frac{\varepsilon_3^* - \varepsilon_2^*}{\varepsilon_3^* + 2\varepsilon_2^*}\right)}{\left(\frac{r_2}{r_3}\right)^3 - \left(\frac{\varepsilon_3^* - \varepsilon_2^*}{\varepsilon_3^* + 2\varepsilon_2^*}\right)} \tag{3.12}$$

These two equations present the calculation of the complex permittivity of the cell membrane and cell nucleus for the two-shell model. The geometry of this two-shell model was shown in figure 3.2.4. This model is designed based on the Yeast cell biological structure including cells walls, membrane, and nucleus.

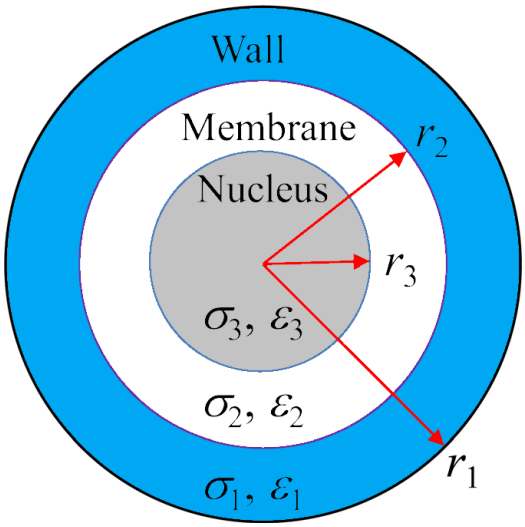

Figure 3.3.2 Two-shell model of Yeast cell considering different dielectric properties for the cytoplasm and membrane, modified from [76].

A more complex overlay multi-shell model can be applied to a CHO cell. There is a nuclear envelope outside the cell nucleus and membrane that can be seen as the shell for the nucleoplasm and cytoplasm. Therefore, a double-shell and double-layer model of CHO cells were designed based on the biologically simplified geometry indicated below:

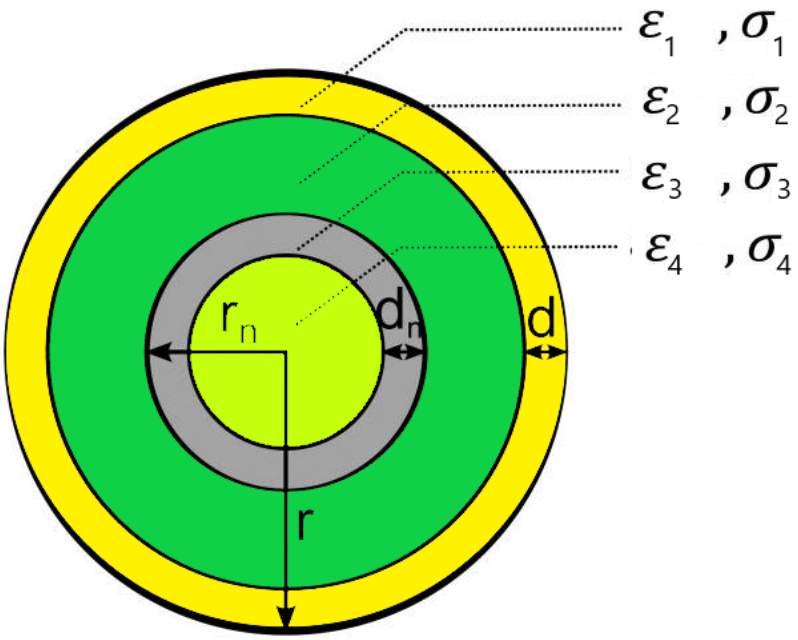

Figure 3.3.3 Multi-shell model of CHO cell considering different dielectric properties for the cytoplasm and nucleoplasm with two shells modified from [77].

The equations (3.11) and (3.12) were extended and derivated into equation (3.13), which can be employed to calculate the complex dielectric constant of the third and the fourth layer.

$$\varepsilon_{34}^{*}=\varepsilon_{2}^{*}\frac{\left(\frac{r_n}{r_n-d_n}\right)^3+2\left(\frac{\varepsilon_4^{*}-\varepsilon_3^{*}}{\varepsilon_4^{*}+2\varepsilon_3^{*}}\right)}{\left(\frac{r_n}{r_n-d_n}\right)^3-\left(\frac{\varepsilon_4^{*}-\varepsilon_3^{*}}{\varepsilon_4^{*}+2\varepsilon_3^{*}}\right)}=\varepsilon_{2}^{*}\frac{\left(\frac{r_3}{r_4}\right)^3+2\left(\frac{\varepsilon_4^{*}-\varepsilon_3^{*}}{\varepsilon_4^{*}+2\varepsilon_3^{*}}\right)}{\left(\frac{r_3}{r_4}\right)^3-\left(\frac{\varepsilon_4^{*}-\varepsilon_3^{*}}{\varepsilon_4^{*}+2\varepsilon_3^{*}}\right)} \tag{3.13}$$

3.4 Clausius-Mossotti factor

The Clausius-Mossotti (CM) factor is one of the most important terms in the DEP force expression. The principle of the CM factor indicated by equation (3.3) highly depends on the dielectric properties of the medium solution and particles. In this thesis, we mainly focused on four types of particles, that is plastic beads, Yeast cells, HEK 293 cells, and CHO_7 cells. These four types of micro-particles can each be modeled by employing the models mentioned above. For medium solution, the thesis work starts from the basic and common solutions to the specific solutions for the adjustment of the CM factor. To adjust the CM factor character during a frequency sweeping of the microfluidic system, to find out the adapt frequency for both capture and detection purpose.

3.4.1 CM factor of a plastic bead in the DI water

For a plastic bead, a simple model could be utilized; its CM factor can be calculated by the equation (3.3).

$$f_{CM} = (\varepsilon_p^* - \varepsilon_m^*)/(\varepsilon_p^* + 2\varepsilon_m^*) \quad (3.3)$$

The complex permittivity of the medium solution and the plastic bead can be calculated by equations (3.7) and (3.8), where the simulation starts from the medium as deionized water. The Dielectric properties of the polystyrene bead and deionized water are shown in Table 3.1.

	Value	Unit
Dielectric constant of Polystyrene bead	2.6	1
Dielectric constant of deionized water	78.5	1
Conductivity of Polystyrene bead	4.80E-4	S/m
Conductivity of deionized water	2.00E-4	S/m

Table 3.1 Dielectric properties of polystyrene bead and deionized water [79]

The real part of the CM factor was simulated by *Matlab R2018a.* Figure 3.4.1 shows how Re(f_{cm}) varies against the frequency in the range from 1Hz to 100MHz.

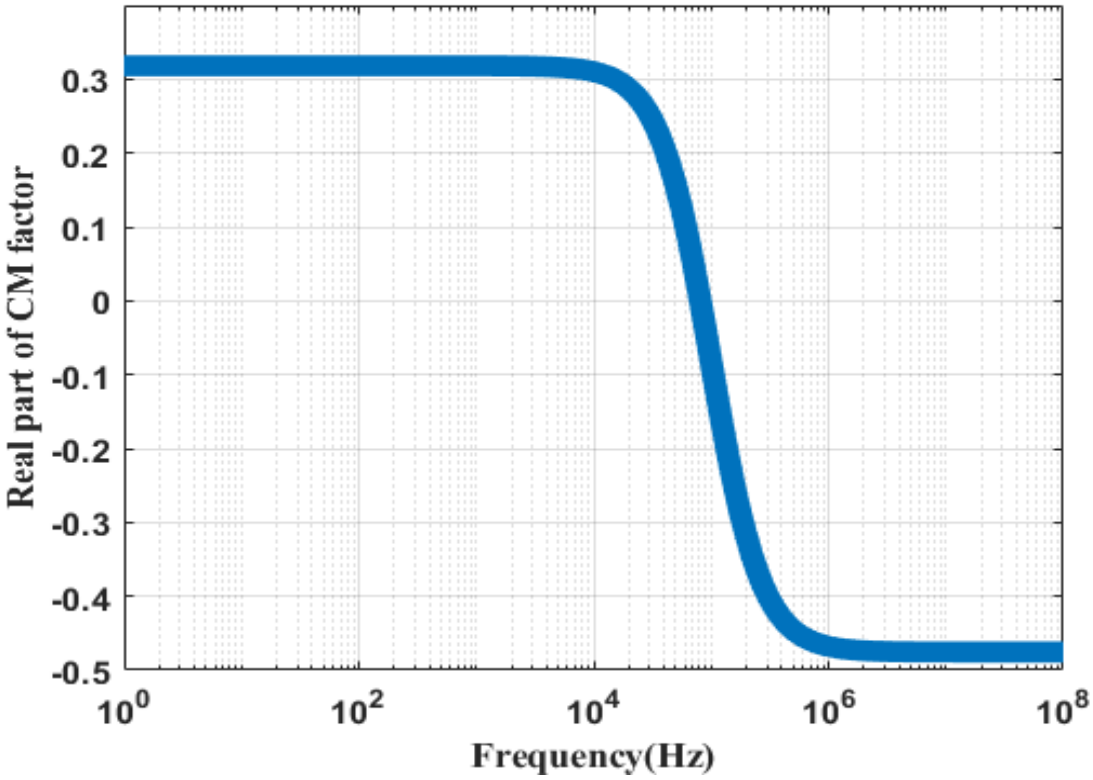

Figure 3.4.1 The real part of the CM factor for the zero-shell model of a Polystyrene bead in DI water.

The case in Figure 3.4.1 shows that the crossover frequency is 7×10^4 Hz. When the frequency was taken below 7×10^4 Hz, pDEP was performed on the plastic bead suspending the DI water.

3.4.2 CM factor of a HEK 293 cell in the DI water

For a HEK 293 cell, a single-layer model as discussed before could be utilized. Where equation (3.9):

$$\varepsilon_p^*(\omega)=\varepsilon_m^*\frac{\left(\frac{R}{r}\right)^3+2\frac{\varepsilon_o^*-\varepsilon_i^*}{\varepsilon_0^*+2\varepsilon_i^*}}{\left(\frac{R}{r}\right)^3-\frac{\varepsilon_0^*-\varepsilon_i^*}{\varepsilon_0^*+2\varepsilon_i^*}} \tag{3.9}$$

The dielectric properties, used to determine the dielectrophoresis behavior of HEK 293 cells in the DI water, are referenced in Table 3.2 below [79]:

Parameter	Value
Cell diameter	12.5 um
Membrane thickness	7 nm
Cytoplasm conductivity	0.5 S/m
Cytoplasm relative permittivity	60
Membrane conductivity	7e-14 S/m
Membrane relative permittivity	9.5
Deionized water permittivity	78.5
Deionized water conductivity	2e-4 S/m

Table 3.2 Geometric and dielectric properties of viable HEK 293 cells [79].

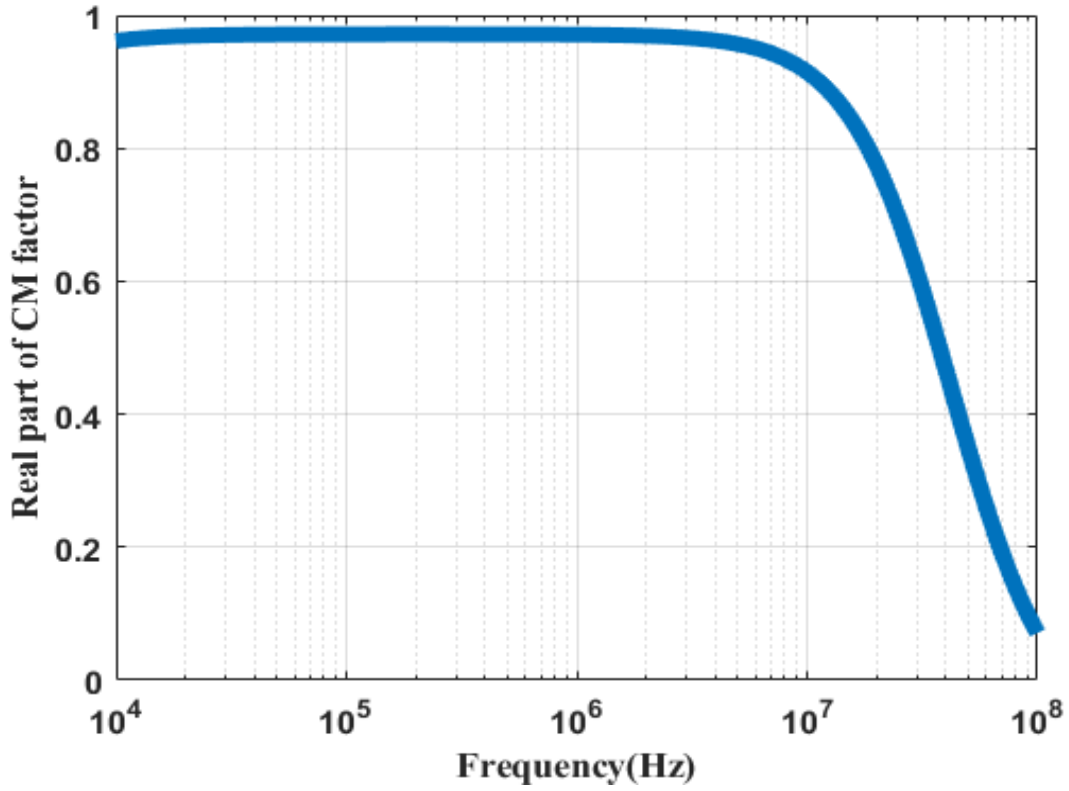

Figure 3.4.2 The real part of the CM factor for the single-shell model of a HEK

293 cell in DI water.

Figure 3.4.2 shows the characters of the Re(f_{CM}) for the case of a HEK 293 cell in DI water. The frequency ranges from 10kHz to 100MHz, and the first crossover frequency would occur over 100MHz. Regarding the simulation results, crossover frequency comes out at a relatively high frequency, while the DEP force is positive on the HEK 293 cells before 100MHz.

3.4.3 CM factor of the Yeast cell in the DI water

To determine the CM factor of the yeast cell, the double-shell model is used in the Matlab simulation, where the model is built up based on equation (3.11) and (3.12).

$$\varepsilon_c^* = \varepsilon_1^* \frac{\left(\frac{r_1}{r_2}\right)^3 + 2\left(\frac{\varepsilon_{23}^* - \varepsilon_1^*}{\varepsilon_{23}^* + 2\varepsilon_1^*}\right)}{\left(\frac{r_1}{r_2}\right)^3 - \left(\frac{\varepsilon_{23}^* - \varepsilon_1^*}{\varepsilon_{23}^* + 2\varepsilon_1^*}\right)} \tag{3.11}$$

And

$$\varepsilon_{23}^* = \varepsilon_2^* \frac{\left(\frac{r_2}{r_3}\right)^3 + 2\left(\frac{\varepsilon_3^* - \varepsilon_2^*}{\varepsilon_3^* + 2\varepsilon_2^*}\right)}{\left(\frac{r_2}{r_3}\right)^3 - \left(\frac{\varepsilon_3^* - \varepsilon_2^*}{\varepsilon_3^* + 2\varepsilon_2^*}\right)} \tag{3.12}$$

To model viable yeast cells, the geometric and dielectric properties shown below were referenced:

Parameter	Value
Cell diameter	8um
Membrane thickness	8nm
Wall thickness	220nm
Cytoplasm conductivity	0.2 S/m
Cytoplasm relative permittivity	50
Membrane conductivity	25e-8 S/m
Membrane relative permittivity	6
Wall conductivity	14e-3 S/m
Wall relative permittivity	60

Table 3.3 Geometric and dielectric properties of viable yeast cells [80].

The real part of the CM factor when a Yeast cell is suspended in DI water and the result is shown in Figure 3.4.3. The crossover frequency was figured out regarding the result as 4×10^{7} Hz. Therefore, during frequency range from 100Hz to 4×10^{7} Hz, yeast cells will be affected by the pDEP force.

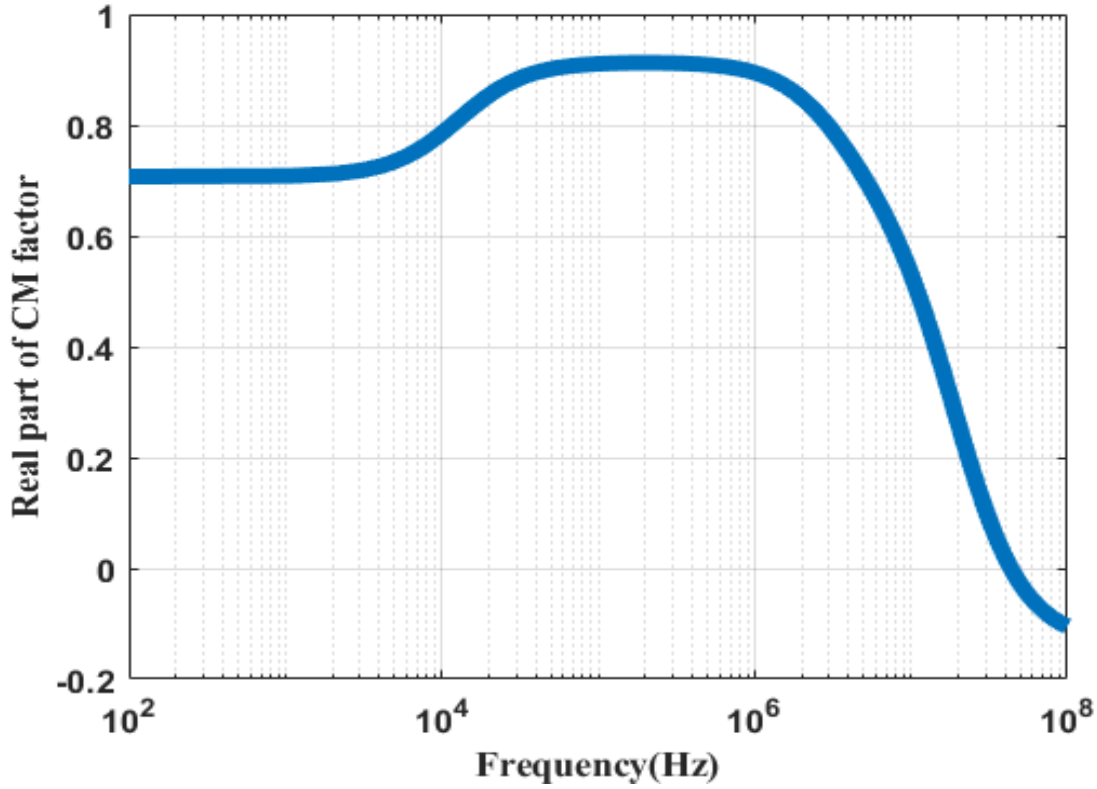

Figure 3.4.3 The real part of the CM factor for the double-shell model of a yeast cell in DI water.

3.4.4 CM factor of the CHO_7 cell in the DI water

The multi-shell model, regarding the CHO cell biological structure, will be employed for CHO_7. The equation 3.13 was involved in the simulation to get the model of the third and the fourth layer, which were seen as the cell's membrane and cytoplasm. For the multi-shell model of a CHO cell, the dielectric properties are given in table [77]:

Parameter	Value
Cell diameter	6um
Membrane thickness	5nm
Nucleus radius	3.3um
Nuclear envelope thickness	40nm

Cytoplasm conductivity	0.42 S/m
Cytoplasm relative permittivity	60
Membrane conductivity	1e-6 S/m
Membrane relative permittivity	8.5
Nucleoplasm conductivity	1.50 S/m
Nucleoplasm permittivity	120
Nuclear envelope conductivity	1e-3S/m
Nuclear envelope permittivity	23.2

Table 3.3 Geometric and dielectric properties of viable CHO_7 cells [77].

The real part of the CM factor was simulated when a CHO_7 cell was suspended in DI water; the result obtained is shown in Figure 3.4.4. The crossover frequency of the CHO_7 cell does not come out in the frequency range from 100Hz to 100MHz. The CHO_7 cell was affected by pDEP during the entire frequency sweeping.

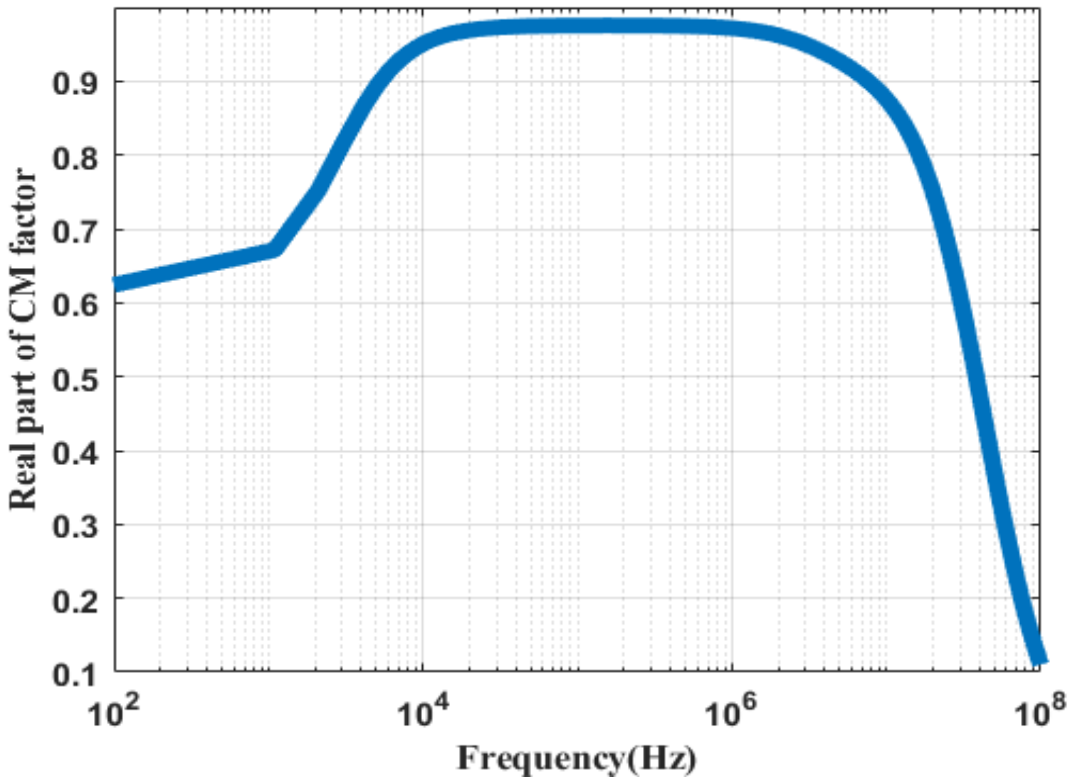

Figure 3.4.4 The real part of the CM factor for the multi-shell model of a CHO cell in DI water.

Overall, one purpose of this thesis is to simulate and figure out the frequency at which the capture process of a target cell in a micro-particle medium with multiple species can be achieved. A HEK 293 cell was selected as the target cell to be captured among the four micro-particles in the same medium. The pDEP force can be employed to attract the target micro-particle to the electrode edges and the nDEP force can help repel the interferential micro-particle away from the electrode. Therefore, it is important to find the critical frequency that can allow the pDEP effect on HEK 293 cells and the nDEP effect on the Polystyrene beads, Yeast cells, and CHO cells. Figure 3.4.5 shows the combined results of the four micro-particles; the blue line shows the Re(f_{CM}) of polystyrene beads, the red line shows the Re(f_{CM}) of HEK 293 cells, the yellow line shows the Re(f_{CM}) of Yeast cells, and the purple line shows the Re(f_{CM}) of CHO cells. To achieve the capture and separate goals

synchronously, the frequency range was selected where the Re(f_{CM}) of the plastic bead, Yeast cell, and CHO_7 cell was below zero and that of the HEK 293 cell was above zero. Thus, the pDEP force will be applied on the HEK 293 cells and the nDEP force will be applied on the plastic beads, Yeast cells, and CHO cells at the same time. The target cell will split from the other particles and will finally be captured by the electrode digits.

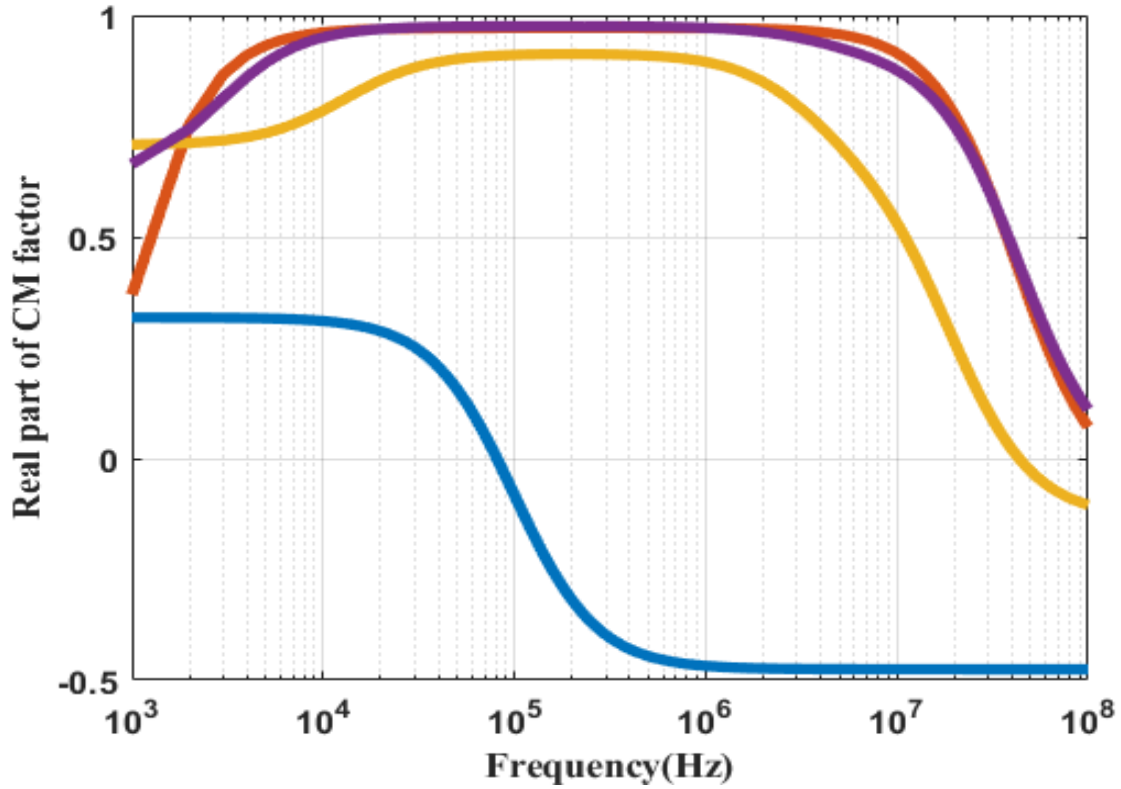

Figure 3.4.5 The real part of the CM factor response against the frequency of polystyrene bead (blue), HEK 293 cell (red), yeast cell (yellow) and CHO_7 (purple) when suspended in the DI water.

3.5 Adjustment of medium solution conductivity

As shown in Figure 3.4.5, the desired frequency did not appear. The blue and yellow lines have a significant drop when the frequency is increased, but the purple and red lines are approaching each other. Moreover, for both the blue and yellow lines to go below zero, the frequency has to be at a quite high level. This high and narrow frequency range is not good for impedance detection and circuit complexity. Considering the power consumption and circuit design, when a higher frequency is requested, larger power consumption and more powerful circuit elements are required. There is a way to improve this situation by adjusting the dielectric property of the medium. The former simulations were done with the micro-particle suspended in DI water. The following simulations will show how the conductivity changes have an effect on the real part of the CM factor performance. By adjusting the initial LEC buffer with the addition of PBS [77], the medium conductivity was changed to 200 µS/cm, 400 µS/cm, and 1000µS/cm. The real part of the CM factor changes following the increase in buffer conductivity from 200 to 1000 µS/cm. Figure 3.5.1 to Figure 3.5.3 show the Re(f_{CM}) when four different kinds of micro-particles were suspended in Pbs with conductivity 200 µS/cm, 400 µS/cm, and 1000µS/cm.

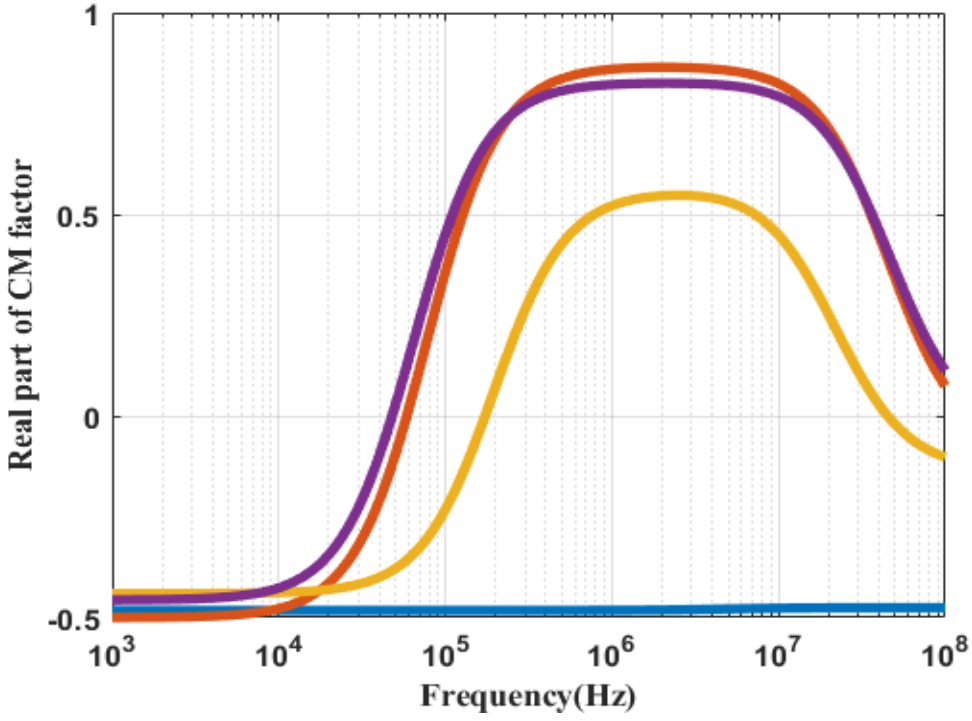

Figure 3.5.1 The real part of the CM factor response against the frequency of polystyrene bead (blue), HEK 293 cell (red), yeast cell (yellow), CHO (purple) when suspended in the buffer solution with 200 µS/cm conductivity.

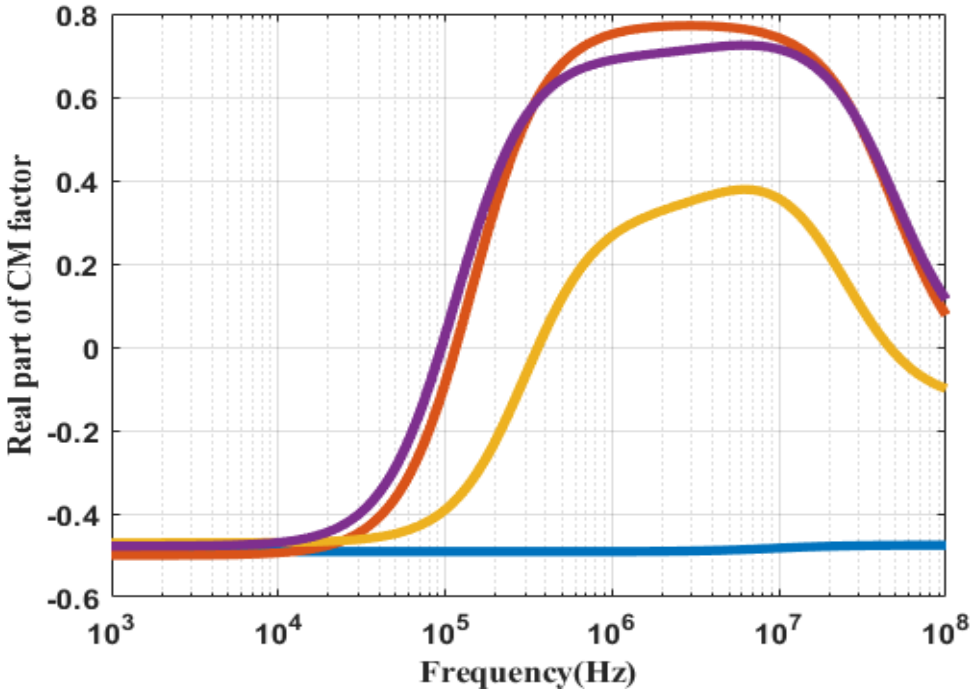

Figure 3.5.2 The real part of the CM factor response against the frequency of polystyrene bead (blue), HEK 293 cell (red), yeast cell (yellow), CHO (purple) when suspended in the buffer solution with 400 µS/cm conductivity.

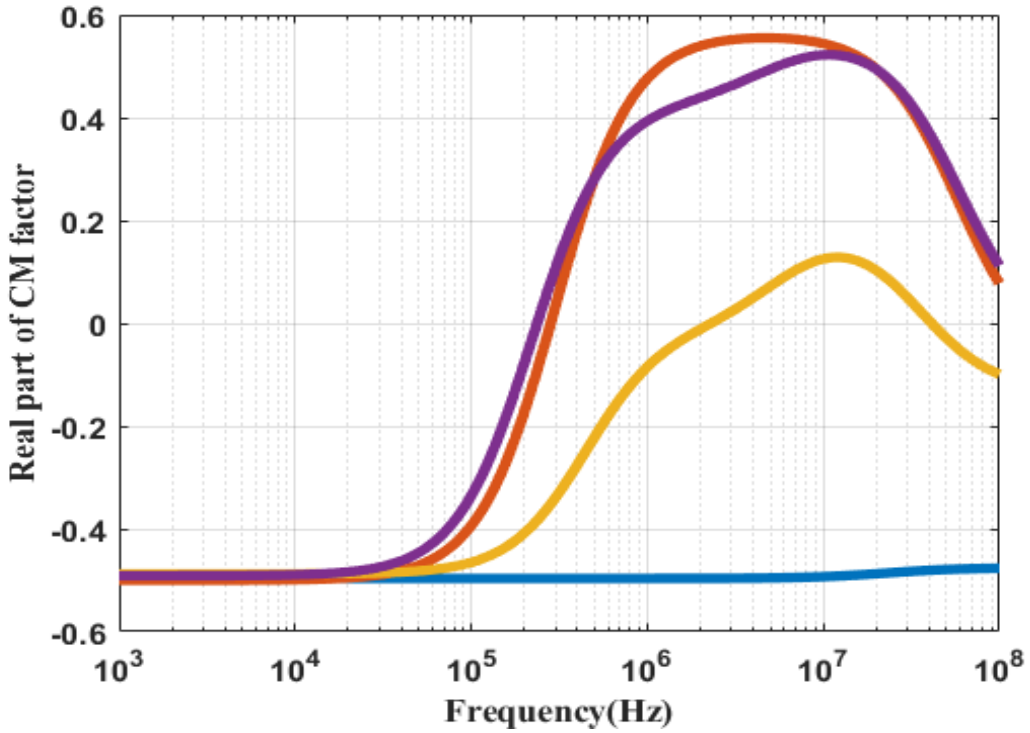

Figure 3.5.3 The real part of the CM factor response against the frequency of polystyrene bead (blue), HEK 293 cell (red), yeast cell (yellow), CHO (purple) when suspended in the buffer solution with 1000 µS/cm conductivity.

The expected frequency range was not yet displayed as can be seen in the above figures. However, there is a significant restriction on the plastic bead and yeast cell. The slight separation between the HEK cell and CHO_7 cell appeared among the frequency range 600kHz to 10MHz. Therefore, the next attempt simulations were done by continuing increasing the conductivity of PBS to a higher level; the results of this are shown below:

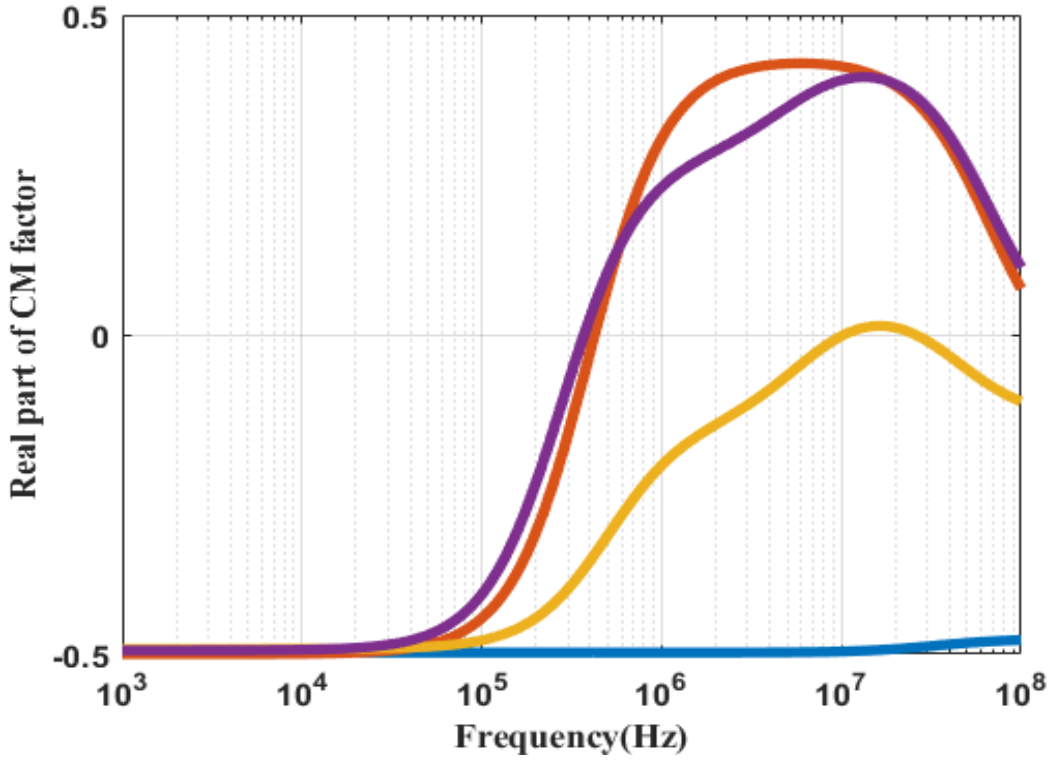

Figure 3.5.4 The real part of the CM factor response against the frequency of polystyrene bead (blue), HEK 293 cell (red), yeast cell (yellow), CHO (purple) when suspended in the buffer solution with 1500 µS/cm conductivity.

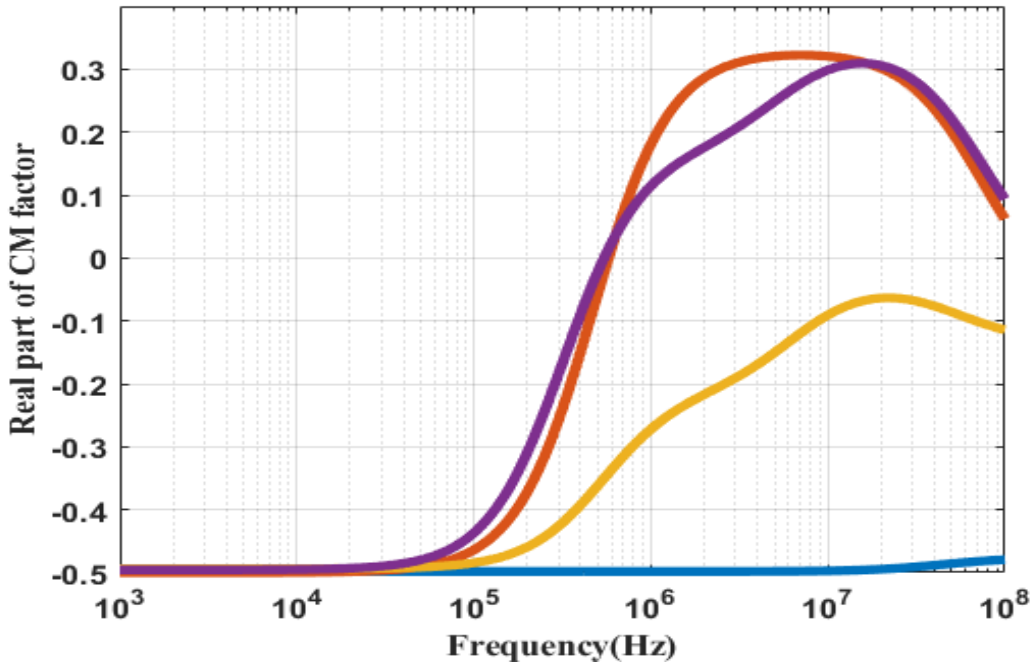

Figure 3.5.5 The real part of the CM factor response against the frequency of polystyrene bead (blue), HEK 293 cell (red), yeast cell (yellow), CHO (purple) when suspended in the buffer solution with 2000 µS/cm conductivity.

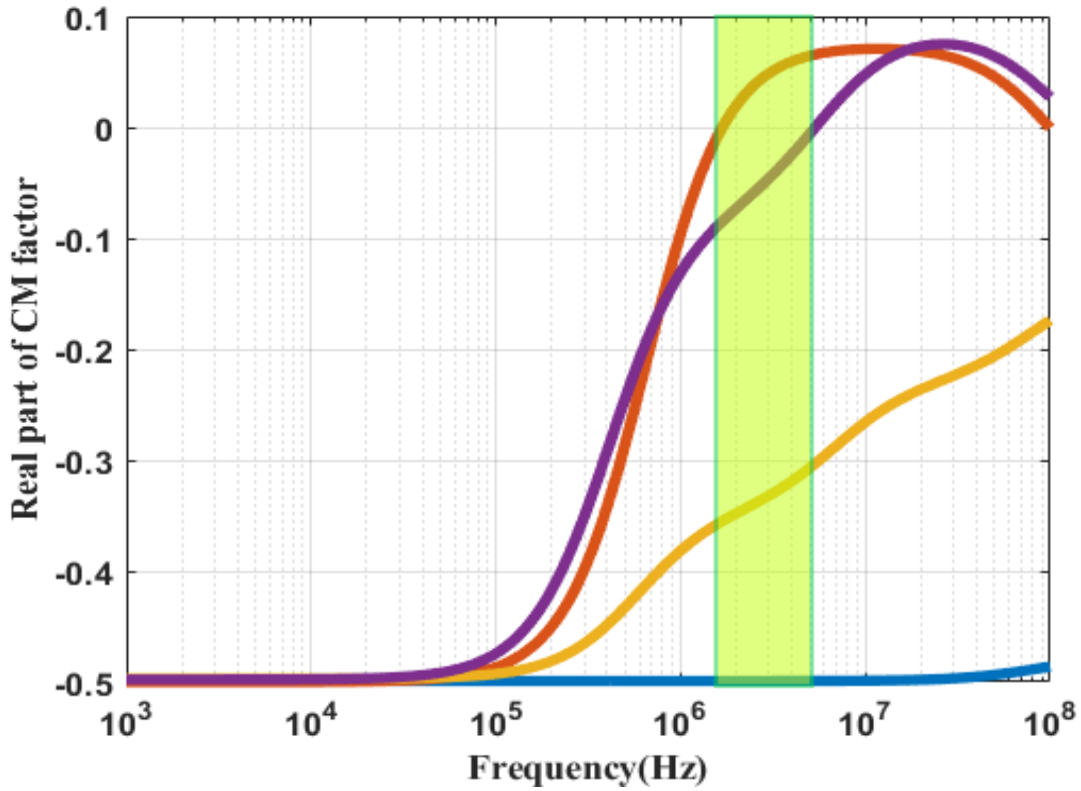

Figure 3.5.6 The real part of the CM factor response against the frequency of polystyrene bead (blue), HEK 293 cell (red), yeast cell (yellow), CHO (purple) when suspended in the buffer solution with 4000 µS/cm conductivity.

According to Figure 3.5.4, Figure 3.5.5, and Figure 3.5.6, the simulation results show the real part of the CM factor of four micro-particles that faced a deep restriction by the change in medium conductivity from 1500 to 4000 µS/cm by adding PBS. The peak value of the real part of the CM factor for both a Yeast cell and a HEK 293 cell dropped significantly when the conductivity was increased. Additionally, the expected separate frequency appeared, which ranged from 5×10^5 to 1×10^7 (Green highlight region). During this frequency region, only the HEK 293 cell was affected by pDEP

and got captured by the IDEs system, while the other particles were repelled away. Thus, when the medium conductivity is 4000 μS/cm, an ideal split frequency range is present. Another consideration of the detection process will be discussed in the future chapter. A high conductivity made from a high concentration of salinity can be toxic to cells [81], which will be discussed in the ongoing work as well.

3.6 Cell capture in DI water (verification)

The cell capture process was simulated using COMSOL Multiphysics 5.3a, which is a powerful multi-physics based simulation software. It combines "AC/DC", "creeping flow", and "particle tracing modules" to simulate the capture and separate process in this thesis. As shown above, in Figure 3.4.5, using water as the buffer medium cannot split HEK 293 cells from the other three cells. Although the separation of the target cells could not be achieved in the DI water, this simulation was done for the verification of the former principal and the theory of DEP. Four different models were also employed in this simulation, and the simulation result can visually present the particle movement and capture condition. Therefore, one test AC signal with a frequency of 1 kHz and a voltage magnitude of 1V peak-to-peak was applied to the IDEs system. The expected result for this signal and the IDEs system is that a pDEP force will be applied on all the four micro-particles according to Figure 3.4.5; the simulation results are shown in Figure 3.6.1.

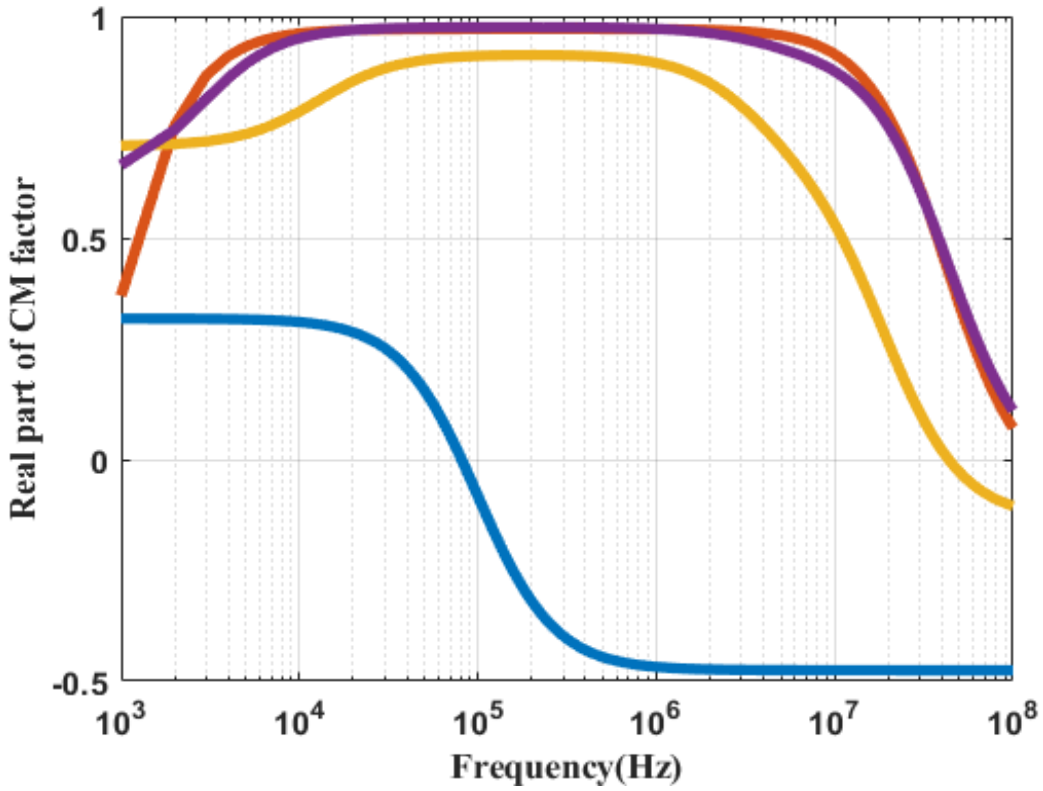

Figure 3.4.5 The real part of the CM factor response against the frequency of polystyrene bead (blue), HEK 293 cell (red), yeast cell (yellow) and CHO_7 (purple) when suspended in the DI water.

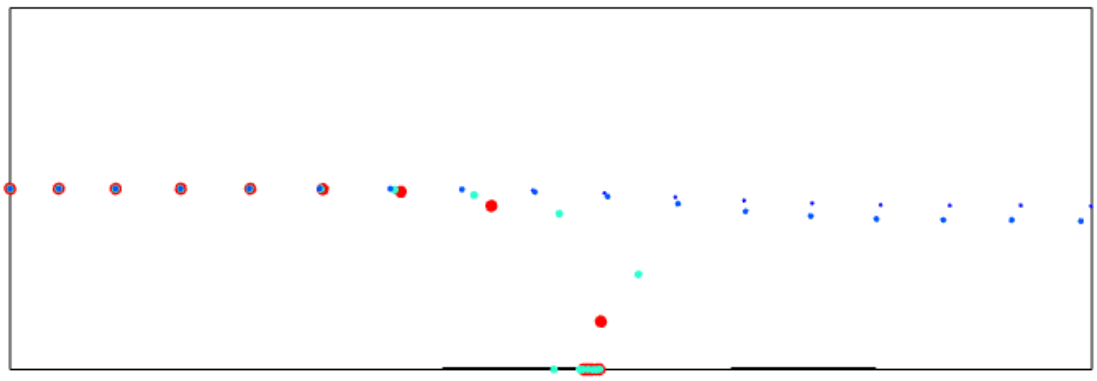

Figure 3.6.1 COMSOL particle tracing simulation results at 1kHz for particles in DI water.

Figure 3.6.1 shows the movement of four kinds of micro-particles in the microfluidic IDEs system when the frequency was given at 1kHz. According to the responding CM factor character curve shown in Figure 3.4.5, it is expected that all

four types of particles were supposed to be captured by the pDEP force at 1kHz. However, this simulation shows a different condition of the particle movement. Only the HEK 293 cells (Red) and the yeast cells (Mint) are captured in this plot. It can still be seen that the CHO cells (light blue) and the Plastic beads (dark blue) were affected by pDEP, lowering them a little bit towards the electrodes. Therefore, it is necessary to explore the other factors that were affected by the movement for cell capture and separation. For instance, the flow rate and size of the particle will make an impact on the drag force, which mainly supports the particle motion in the direction of the x-axis. To show the impact made by the magnitude of the CM factor, another test was applied with a frequency at 1MHz, and the simulation results are shown in Figure 3.6.2.

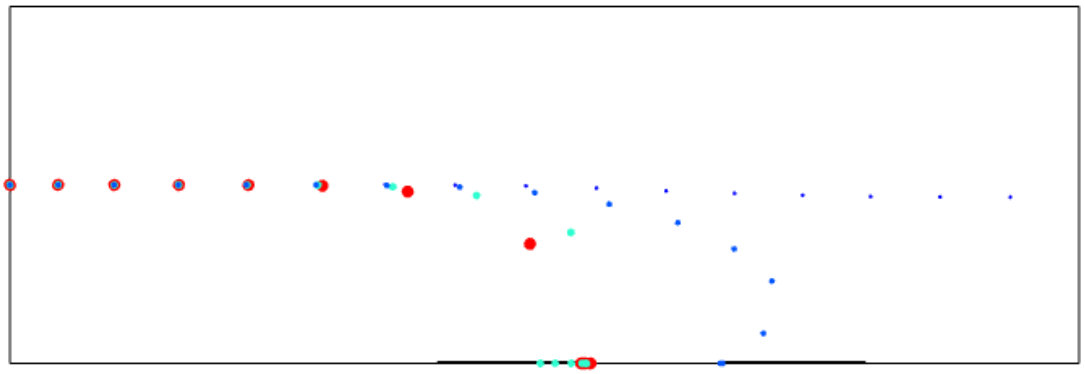

Figure 3.6.2 COMSOL particle tracing simulation results at 1MHz for particles in DI water.

Compared to the simulation results in Figure 3.6.1, which was done at 1kHz, the Yeast cells got captured by the edge of the right electrode. This was caused because the magnitude of the real part of the CM factor increased from around 0.6 to 0.8. Therefore, a larger pDEP force was applied to the particle, in turn, changing the movement track.

3.7 Conclusion

In this chapter, two types of DEP forces and the CM factor of the DEP force were introduced and explored. The CM factors of four micro-particles in the different conditions have been discussed in detail. The medium solution conductivity was adjusted to get an appropriate character curve of the CM factor, which can provide different types of DEP force on the target particles. The COMSOL simulation results demonstrate the ability of an IDE system to capture cells. Finally, the simulation results indicate that the DEP force is affected by the magnitude of the CM factor and there are other factors that affected the movement of particles. Overall, to capture the target cells or split the target cells from a bunch of micro-particles, the conductivity of the medium and the applied frequency are two controllable factors for the DEP force. More factors that could affect the particle motion such as the particle size and flow rate will be discussed with more detailed simulation results of the movement of the particles through the micro-channel in the next chapter.

Chapter 4 Selected Condition of Particle Capture Separation and Detection

4.1 Principle of the particle momentum

In the previous chapters, the IDE system, the DEP force, and the principle of cell capture were indicated. When the micro-particle is traveling in an IDEs based micro-channel, besides the DEP force, another force—the drag force, given by the flow—affects the particles. For a particle moving in the micro-channel, the momentum can be expressed with Newton's Second Law. The net force on the particle is equal to the momentum change during a unit time, which can be shown as equation 4.1:

$$\frac{d}{dt}(m_p v) = F_D + F_g + F_{ext} \tag{4.1}$$

This is shown visually in Figure 4.1.1:

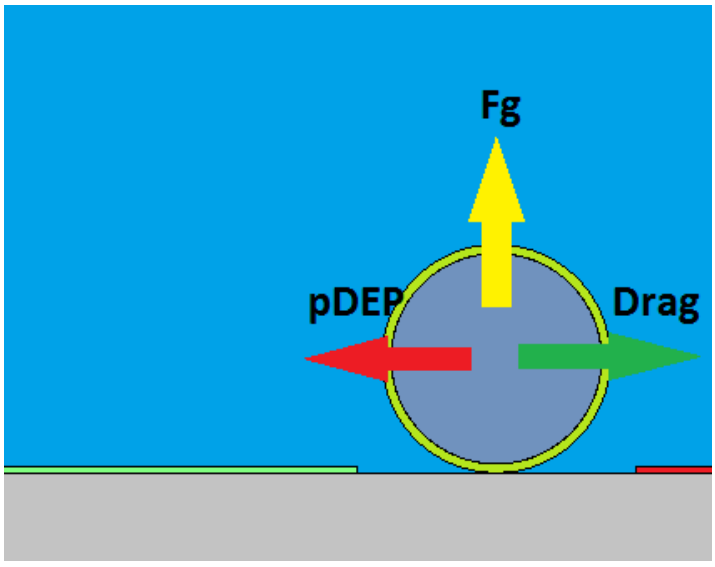

Figure 4.1.1 Net force on a particle during flowing in a microfluidic channel with IDEs system.

In equation (4.1), F_D is the Drag force which can be defined as:

$$F_D = \left(\frac{1}{\tau_P}\right) m_P (u - v) \tag{4.2}$$

Where m_P is the particle mass (SI unit: kg), τ_P is the particle velocity response time (SI unit: s), v is the velocity of the particle (SI unit: m/s), u is the fluid velocity (SI unit: m/s), F_g is the gravitational force vector (SI unit: N), and F_{ext} is any other external force (SI unit: N). The particle velocity response time can be expressed as:

$$\tau_P = \frac{\rho_P d_P^2}{18\mu} \tag{4.3}$$

Where μ is the fluid viscosity (SI unit: Pa s), ρ_P is the particle density (SI unit: kg/m^3), and d_p is the particle diameter (SI unit: m).

The term F_g is the gravity force on the particle, which is given by:

$$F_g = m_P g \frac{(\rho_P - \rho)}{\rho_P} \tag{4.4}$$

Where ρ is the density of the medium fluid and g is the gravity vector. The term F_{ext} is the external force on the particle such as the Dielectrophoretic force in the case of an IDEs system. This force, which was discussed in Chapter 3, is given as:

$$F_{ext} = 2\pi r_P^3 \varepsilon_0 real(\varepsilon_f) real(\frac{\varepsilon_P - \varepsilon_f}{\varepsilon_P - 2\varepsilon_f}) \nabla \left|E_{rms}\right|^2 \tag{4.5}$$

E_{rms} denotes the root mean square electric field. In equation (4.4), the term F_g mainly depends on the density of the medium and particles. During the simulation, all the particle and medium densities ranged from 980 kg/m^3 to 1070 kg/m^3. In cases where there is a slight difference between ρ and ρ_P or a small particle mass, F_g can be ignored since it is close to 0.

As shown in equations 4.2 and 4.3, the diameter of the particle plays an important role in its flow rate, since $F_D \propto \frac{1}{d_P^2}$. Therefore, the particle size will influence the particle momentum. This is especially significant for plastic beads that have a large range of size possibilities. Meanwhile, as $F_{ext} = F_{DEP} \propto r_P^3$, a larger size particle would have a cubic increment of DEP force, which can be a significant way to increase the DEP force. The difference in size between a living and dead cell is an important factor for the cell capture or separation process. This is also proved in the simulation results shown in Figure 3.6.1 in the previous chapter.

Besides particle size, the flow rate plays an important role as well. When the cells are captured by the electrode edge, the DEP force must be balanced with the drag force. If a larger flow rate was applied in the micro-channel, the drag force would increase. Additionally, for the same height from the particle to the electrode in the Y-axis direction, a larger flow rate carries the particle and moves it faster, which is harder to capture during a limited effective distance of the electrical field. Thus, to prevent the particle's secession from the electrode edge during the detection process, a flow rate as slow as possible would be desirable. A design with a larger digit length and channel width can reduce the flow rate.

4.2 Frequency synchronization

The final goal of this IDEs system design is to detect the target cell and define whether the target cell is captured or not. Since the detection signal and capture frequency are used at the same time, the frequency range of the capture frequency is limited. As discussed earlier in Chapter 2, impedance detection in this design is based on the different dielectric properties of micro-particles. The CM factor, which is a highly frequency dependent parameter for the capture process, was discussed in Chapter 3.

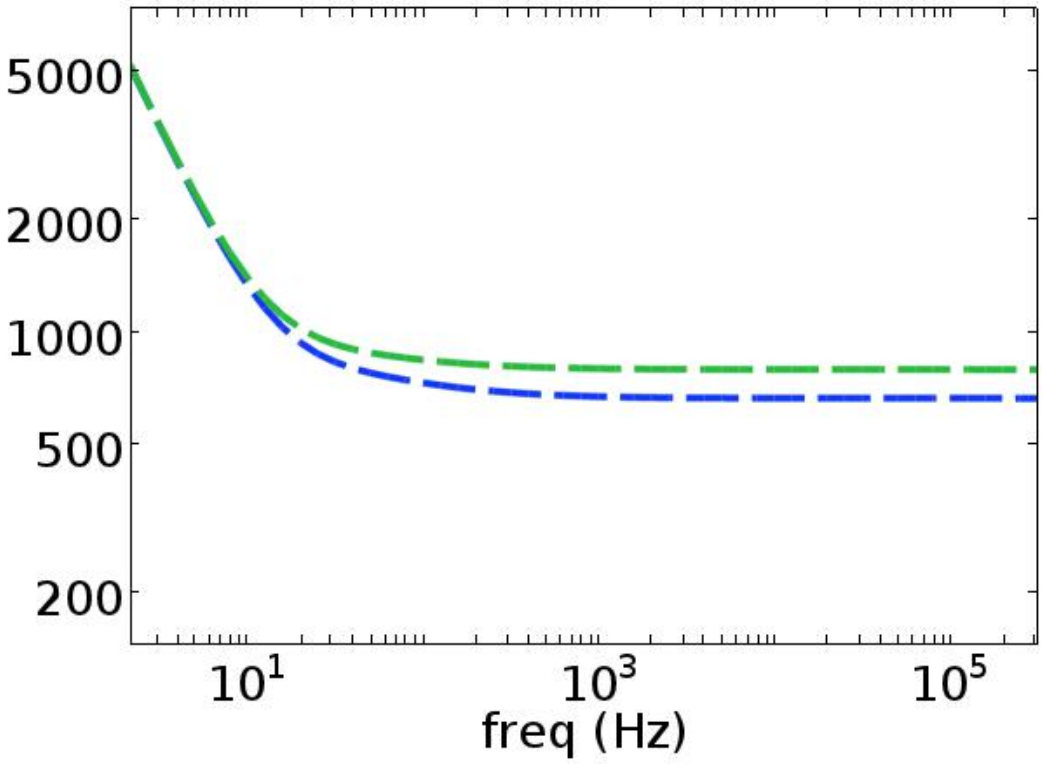

Figure 4.2.1. Impedance responses of plastic bead in the DI water.

The green line in Figure 4.2.1 shows the simulation results of impedance response when a plastic particle was captured at the center of the electrodes' gap in the DE water. The blue line is the impedance response of the electrode in the DI water when there are no particles in the surroundings. The impedance response difference clearly showed up between the frequency ranges from around 1×10^3 to 1×10^5 Hz. As discussed before, by this impedance difference, a detection signal will be generated and read by the detection circuit. Therefore, as a basic and simple instance to explore the DEP capture process, the capture frequency of the plastic bead should be applied within the frequency range where the detection circuit can detect the signal of impedance difference.

4.3 Particle size, Flow rate, and Applied voltage impacts

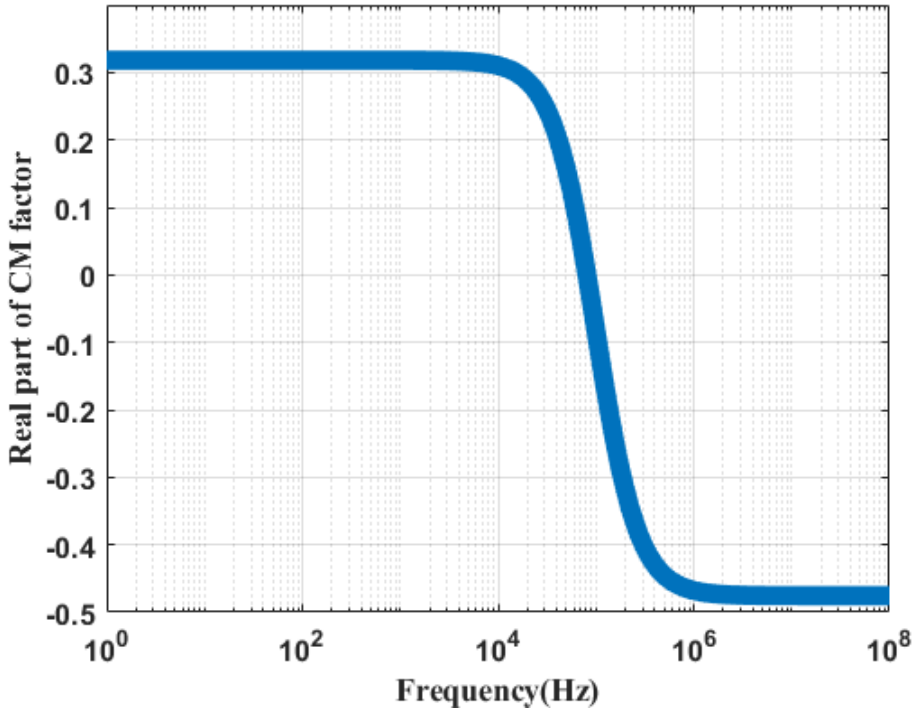

Figure 4.3.1 CM factor of plastic bead in the DI water

As seen in Figure 4.3.1, a pDEP force can be ideally applied when the frequency is lower than 8×10^4 Hz in the DI water and the plastic bead can be captured at 1kHz, which is an ideal frequency for capture goal. The plastic bead was selected as a basic and simple reference model to explore other factors of the particle's movement during the IDEs micro-channel. Then, simulation results of the plastic bead model were used to predict and guide the micro-particle capture and separate process in a more complicated condition. As the result shown in the previous chapter, the particle size and flow rate may highly affect the movement of the plastic bead. The simulations were done to verify the effects in the COMSOL, where the frequency was selected at 1kHz in the DI water.

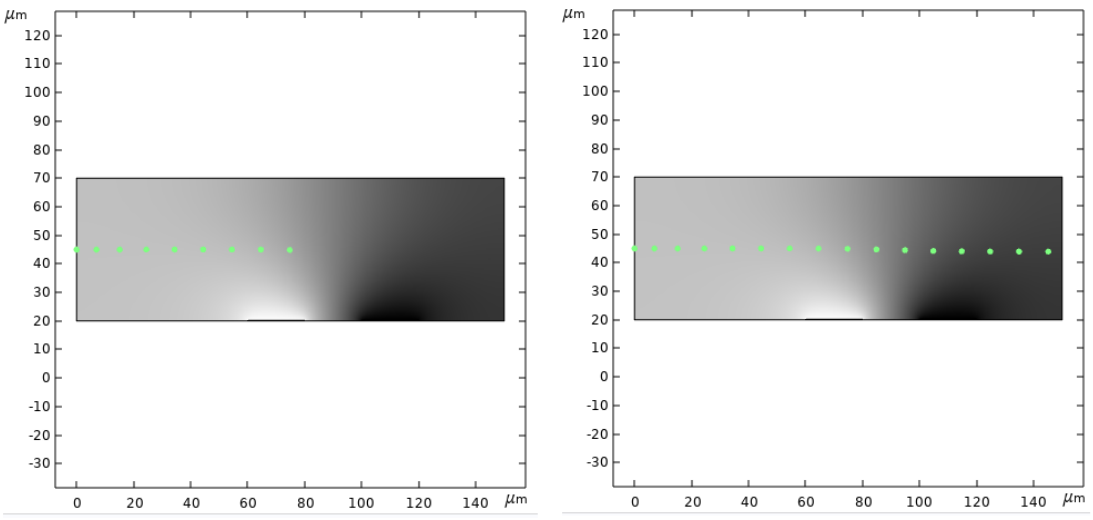

Figure 4.3.2 2 µm radius plastic bead passing through the micro-channel in DI water with 120 µm/s @1kHz, ±1Volt (Vpp).

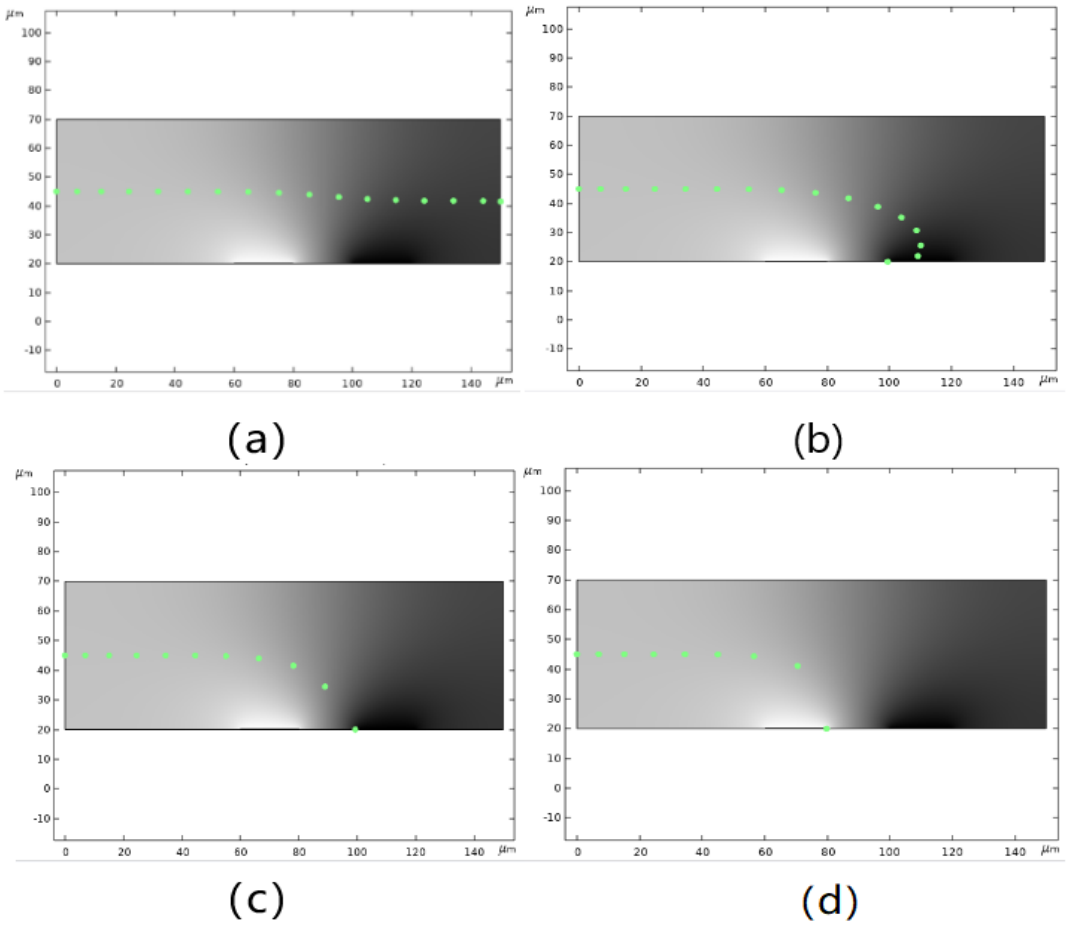

Figure 4.3.3 4 µm (a), 6 µm (b),8 µm (c), 12 µm (d) radius plastic bead passing through the micro-channel in DI water with 120 µm/s @1kHz, ±1Volt (Vpp)

In Figure 4.3.2, the result plots show the plastic bead moving on the track. As the real part of the CM factor curve shown in 4.3.1, it is supposed to be captured by an electrode at 1kHz in the DI water. However, as discussed in section 4.1,

$$F_D \propto \frac{1}{d_P^2}$$

$$F_{ext} = F_{DEP} \propto r_P^3$$

For a plastic bead with radius 2 μm in the DI water where the applied voltage is 1 Volt peak to peak and the frequency of the signal is 1k Hz, it cannot be captured at the 120 μm/s flow rate. The radius of the bead was increased from 2 μm to 12 μm. The simulation results are shown in Figure 4.3.3, which show that a larger size of plastic bead can be more easily captured because of a more effective DEP force and a less effective drag force that will be applied on the plastic bead. When the plastic bead radius was given as 4 μm (shown in Figure 4.3.3(a)), the path of the bead's motion was going down slightly since it was affected by pDEP. When the radius reached 6 μm(b), the path of motion of the bead shows that the bead changed direction after passing the electrode and was eventually captured at the edge of the right electrode. As the radius kept increasing to 8 μm(c), the beads could be directly captured at the edge of the right electrode since the pDEP force is larger as compared to the drag force. In plot (d) with a radius of 12 μm, the beads were easily captured at the edge of the left electrode, which indicates that an even larger pDEP force was present.

As mentioned above, the radius affects the DEP force and drag force in terms of the particle dielectric properties and geometric properties. Another important factor that affects this kinetic system is the flow rate of microfluid, which provides the drag force directly by:

$$F_D = \left(\frac{1}{\tau_P}\right) m_P (u - v) \tag{4.2}$$

At the capture point, F_{DEP} should balance with F_D in this system. Also, there should be

enough time for the DEP force to capture the particle within the effective region before the particle passes by, which is highly relative to the flow rate. Different simulations were applied on the plastic bead when the radius was controlled as 4 µm and also the certain height of the particle position was controlled in the microchannel (25 micrometers in this case).

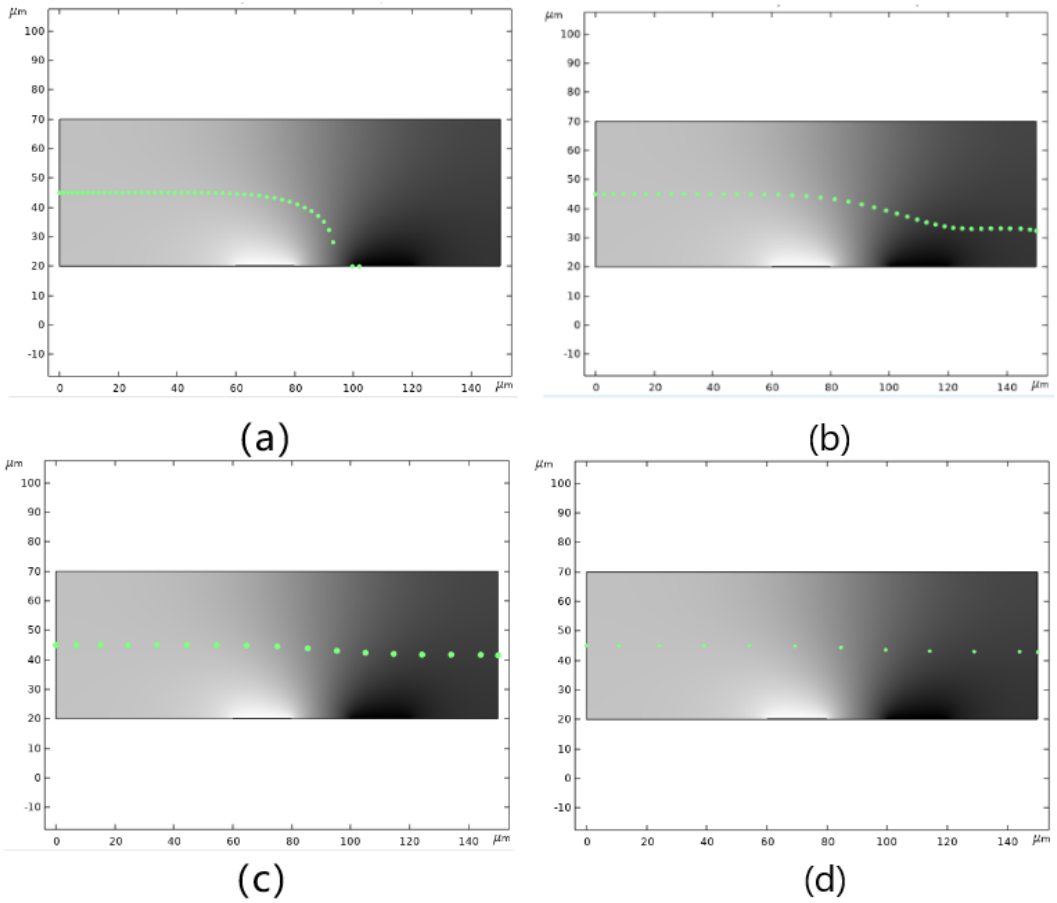

Figure 4.3.4 4 µm radius plastic bead passing through the micro-channel in DI water with 30µm/s (a), 60µm/s(b), 120 µm/s(c), 200µm/s(d) @1kHz, ±1Volt (Vpp).

As expected, a lower flow rate can make the process easy to capture the plastic bead. In plot (a) where the flow rate is 30 µm/s, plastic beads with a radius of 4 µm can be captured at the right electrode edge. As the flow rate increased, the DEP force was relatively low to capture the particle in the effective electrical field region, so the plastic beads could not get captured during the flow rate conditions of the plot (b), (c), and (d).

Another factor of the DEP force is the root mean square electric field E_{rms} (Unit: V/m), where the electrical potential V responsible was the applied voltage of the electrode. Therefore, the peak to peak voltage of the AC supply will also have a significant effect on the DEP force as:

$$F_{ext} = 2\pi r_P^3 \varepsilon_0 real(\varepsilon_f) real(\frac{\varepsilon_P - \varepsilon_f}{\varepsilon_P - 2\varepsilon_f}) \nabla \left| E_{rms} \right|^2 \tag{4.5}$$

$$F_{DEP} \propto \nabla \left| E_{rms} \right|^2$$

For the purpose of capturing living cells and power consumption, a high voltage is not recommended. However, if the microfluidic device is limited in its minimum flow rate it can provide, a reasonably higher voltage can be a way to capture the target micro-particles. For plastic beads, which is kind of like an experimental mouse, simulations were done without consideration of cell survival and effects on temperature.

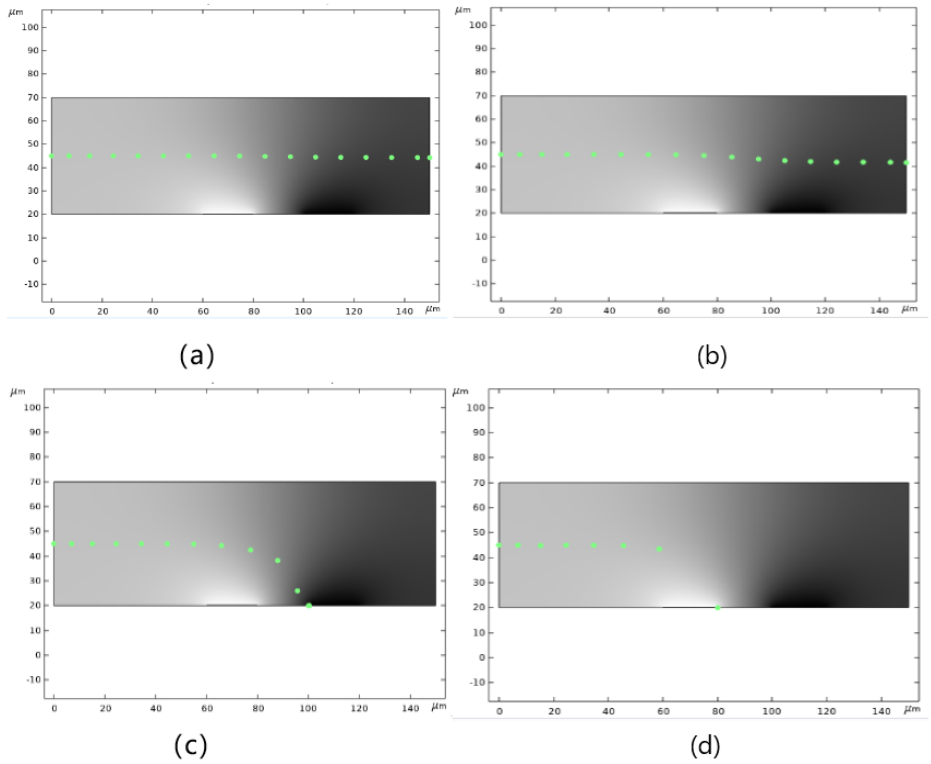

Figure 4.3.5 4 µm radius plastic bead passing through the micro-channel in DI water with 120 µm/s @1kHz, ±0.5V(a), ±1V(b), ±2V(c), ±5V(d).

As discussed before, when the applied voltage doubled, the DEP force increased 4 times and the electrical field also increased. Where dropping down the flow rate from 120 μm/s to 30 μm/s, which is equivalent to increase the applied voltage from ±1V to ±2V. The simulation results in Figure 4.3.5 (c) and (d) showed the plastic bead capture at 120 μm/s by the applied voltage ±2V(c), ±5V(d). Compared to the flow rate control, the applied voltage is an easier and more effective way to get a larger DEP force and particle capture.

Another important factor of the DEP force is the dimension of the IDEs system. The more enlarged the electrode array extension, the larger the DEP force will be. The IDE design will be an ongoing part of this project which will be discussed in further work.

4.4 HEK 293 cell capture and separation

Concluding all theories and principles mentioned before, the best separation frequency was selected at 5MHz for the target HEK 293 cell when the medium solution conductivity was adjusted to 4000 μS/cm. The real part character of the CM factor curve was shown in Figure 3.5.6, and the simulation was done in the COMSOL by the applied multiple physics modules; the capture and separate result plot are shown in Figure 4.4.1:

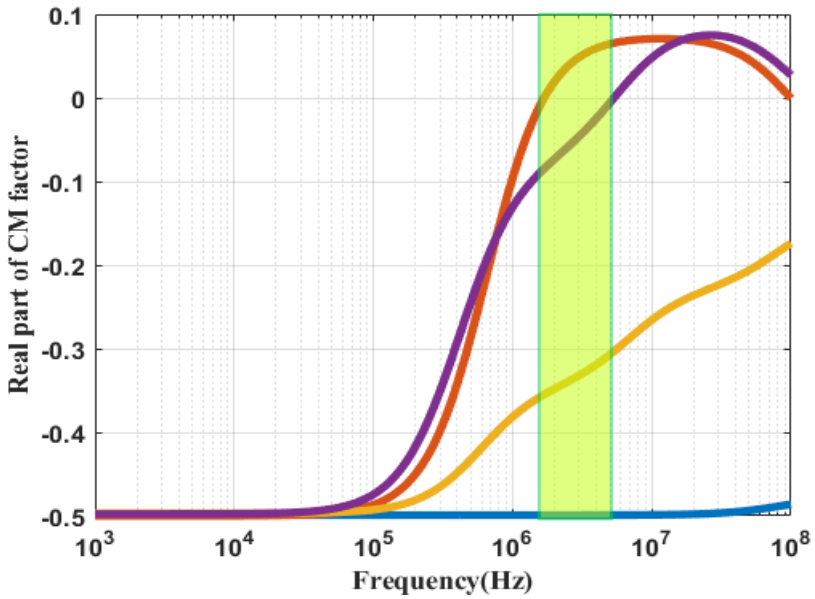

Figure 3.5.6 The real part of the CM factor response against the frequency of polystyrene bead (blue), HEK 293 cell (red), yeast cell (yellow), CHO (purple) when suspended in the buffer solution with 4000 µS/cm conductivity.

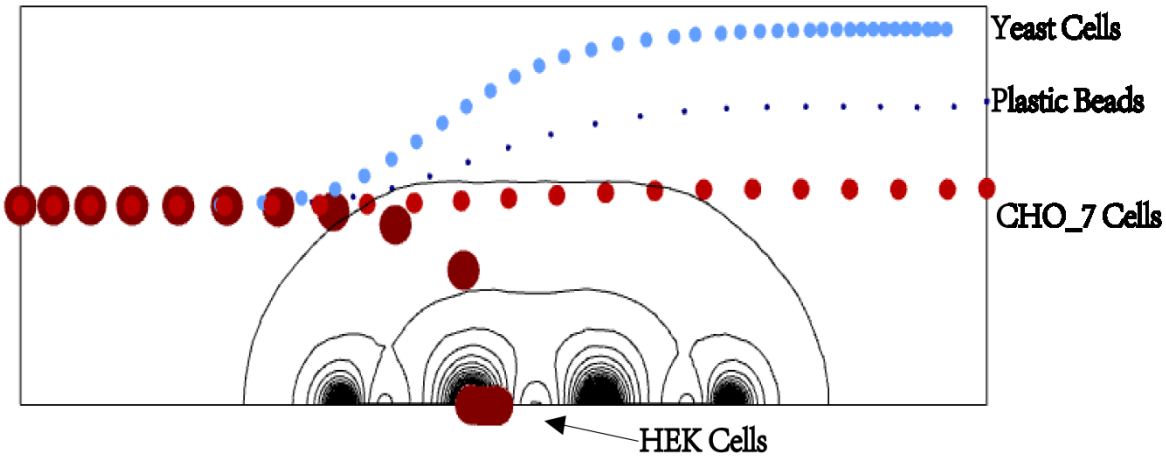

Figure 4.4.1 HEK 293 cells separate from mixed particle group and captured by IDEs system in the microfluidic with 4000 µS/cm at 5MHz.

The results shown above indicate that the system captured the target cells perfectly and repelled all other interferences. To give a larger tolerance for the system

to capture and detect should be developed. Therefore, simulations were done to explore a lower conductivity medium solution and a larger frequency range of capture and detection. Since HEK 293 cells have the largest radius among the four discussed micro-particles, it means it would be more sensitive to the DEP force and less sensitive to the drag force. In Figure 3.5.1, at frequency 100kHz, for instance, plastic beads and Yeast cells would experience an nDEP force while HEK cells and CHO cells would experience a pDEP force. Both the HEK cells and CHO cells have a similar plot for the real part of the CM factor, but the HEK cells are more sensitive to the DEP force and less sensitive to the drag force. The HEK cells can be captured by increasing the flow rate and using a higher voltage to increase the momentum down to the electrode. Despite the CHO cell's slight DEP force, the large drag force would push it towards the outlet of the microchannel. The COMSOL simulation results for this condition are shown in Figure 4.4.2:

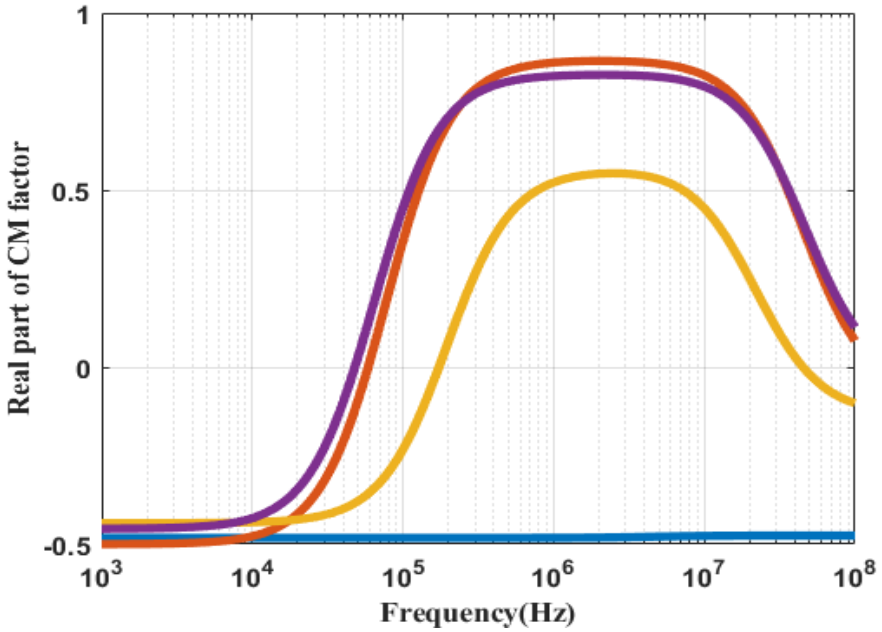

Figure 3.5.1 The real part of the CM factor response against the frequency of polystyrene bead (blue), HEK 293 cell (red), yeast cell (yellow), CHO (purple) when suspended in the buffer solution with 200 µS/cm conductivity.

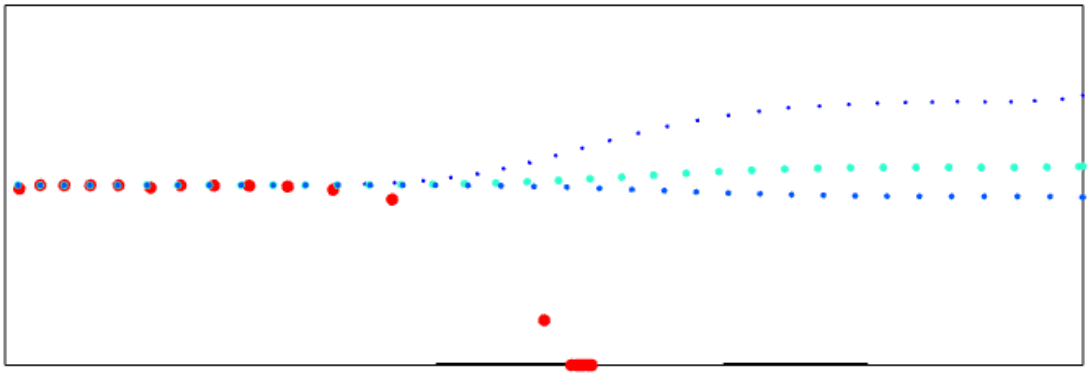

Figure 4.4.2 HEK cell getting captured and separated from the micro-particle group when it was passing through the micro-channel in a 200 µS/cm medium buffer with 60 µm/s @100kHz, ±2V.

By using a higher conductivity medium buffer, capture can be achieved with a lower power supply and faster flow rate to reduce the power consumption of the circuit. Figure 3.5.4 shows the real part of CM factors when the medium buffer conductivity was adjusted to 1500 µS/cm.

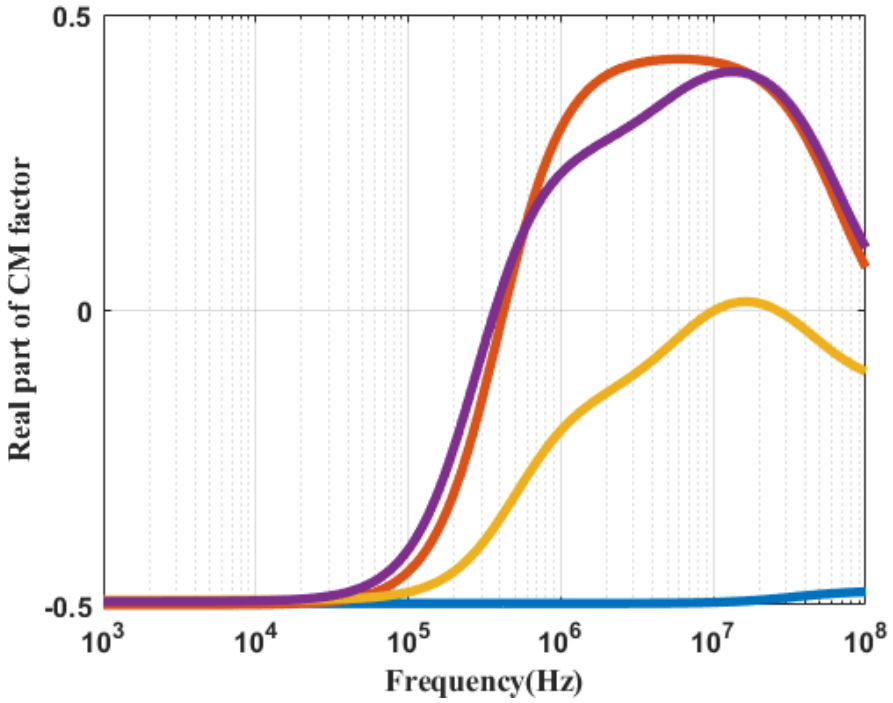

Figure 4.4.3 Real part of CM factor response against the frequency of polystyrene beads (blue), HEK 293 cells (red), yeast cells (yellow), CHO cells (purple) when suspended in the buffer solution with 1500 µS/cm conductivity.

It can be observed that there is a larger difference between the HEK cells and CHO cells in the frequency range from 1MHz to 10MHz. This will reduce the requirements of the power supply to increase the DEP force. However, it will need a larger capture frequency, which is not wanted for circuitry design and detection purposes. Figure 4.4.4 shows the COMSOL simulation results with the conductivity of the medium adjusted to 1500 µS/cm.

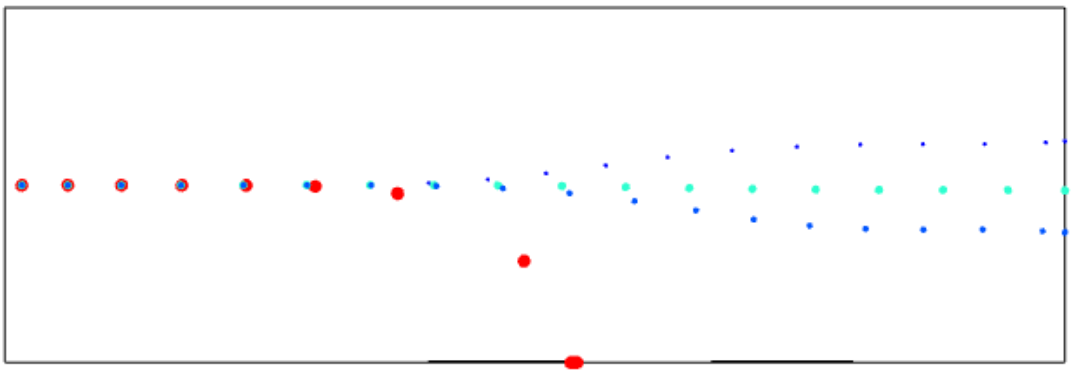

Figure 4.4.2 HEK cell getting captured and separated from the micro-particle group when passing through the micro-channel in 1500 µS/cm medium buffer with 60 µm/s @1MHz, ±2V.

4.5 Cells Detection

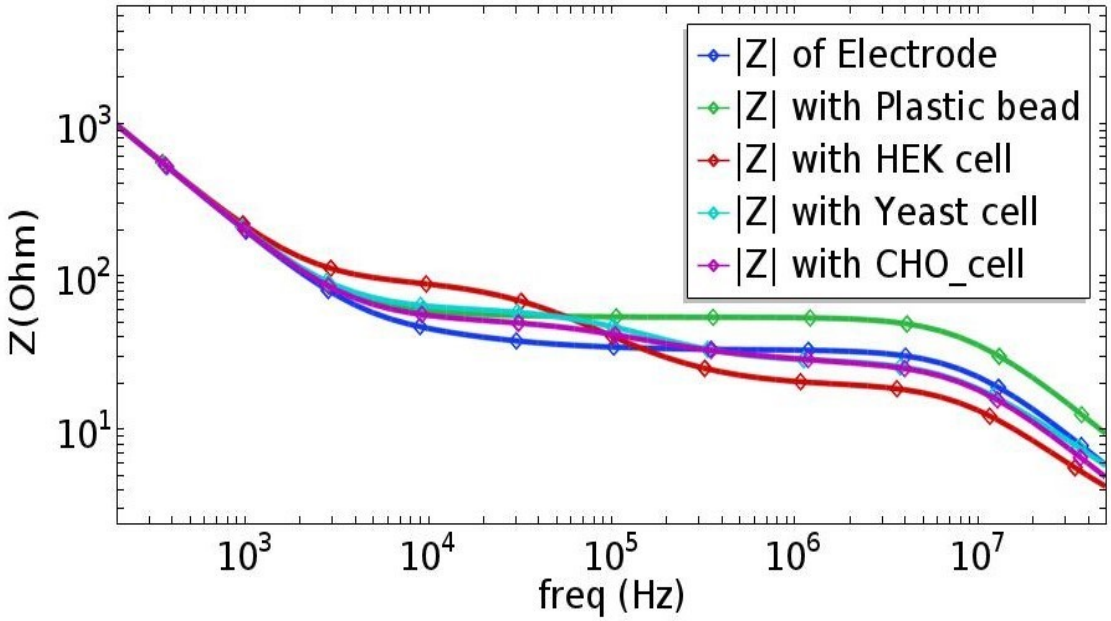

Figure 4.5.1 Impedance Spectroscopy of multi-shell models of a) IDEs system (Blue) b) Plastic bead (Green) c) HEK cell (Red) d) Yeast cell (Mint) e) CHO_7 cell (Purple).

In Figure 4.5.1, simulations were done on the four multi-layer models in the COMSOL. The results show the impedance spectroscopy of the four different types of particles and electrodes. As explored in the previous chapter, regarding the character curve of the real part of the CM factor, the conductivity of the medium solution is selected at the level of 4000 µS/cm. The capture results are perfect and are shown in Figure 4.4.1 in an earlier chapter. The impedance responses are expressed in Figure 4.5.2.

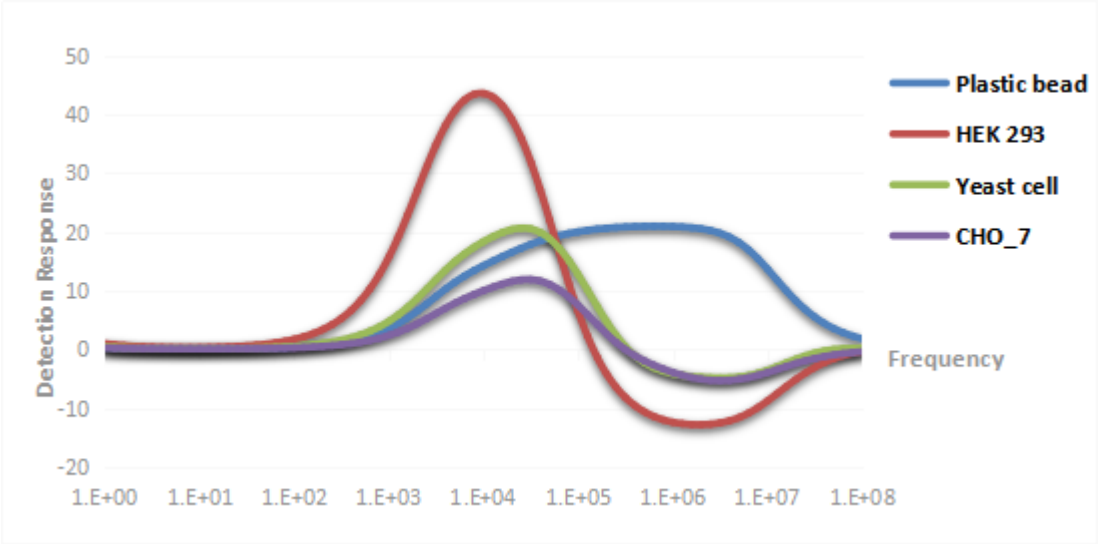

Figure 4.5.2 Detected Impedance response of micro-particles a) Plastic bead (Blue) c) HEK cell (Red) d) Yeast cell (Green) e) CHO_7 cell (Purple).

The applied frequency was selected at 5MHz during the capture process when the medium conductivity was adjusted to 4000 µS/cm. The detected impedance response, shown in Figure 4.5.2, had a significant response of the target cell (HEK 293(red)) in contrast to other micro-particles. The simulation proves that the condition that was set up for cells capture can achieve cell detection at the same time. Additionally, the detection of this process can also tell whether a wrong particle was captured if the detection responses in a different level with the target cells.

4.6 Conclusion

In this chapter, a series of detailed simulations were done by using COMSOL MultiPhysics. The indicated results are as expected from the previous simulations and conclusions. The capture frequency of a HEK 293 cell was selected at 5 MHz with medium solution @ 4000μS/cm, however, this is not the only frequency that can be applied for cell capture. For the purpose of detection, the capture frequency should be selected from the range of 1 kHz to 100 MHz, which is the most applicable frequency range for the impedance detection. The applied voltage should be controlled to as low of a level as possible for the cell liveness. However, increases in voltage is an effective way to increase the DEP force. The particle size is also an important factor for the capture process. As discussed before, for the micro-particle capture, a larger size of the particle is preferred since it can increase the DEP force and decrease the drag force significantly. The size of a plastic bead can be easily controlled. In comparison, it is hard to control the size of a cell. The size can still be a reference when selecting and culturing the cell sample. The size of a cell usually has a range according to the cell maturity. Since the flow rate mainly depends on the equipment such as the fluidic pump, channel width, and microfluidic structure, lots of designs can be used to decrease the flow rate and reduce the drag force. The type of DEP force applied to the different micro-particles is influenced by the selection of the medium solution. Different DEP force performances will be present for different particle and medium combinations. Thus, this thesis expressed the method to capture and separate the target cell from a group of micro-particles with different representative models, by giving a specific and reasonable combination of applied voltage, frequency, flow rate, and medium solution.

Chapter 5 Conclusions and ongoing work

5.1 Conclusions

This thesis work indicated and discussed a biosensor design based on the microfluidic and IDEs system. The goal of the thesis was achieved by simulations in COMSOL and Matlab. It firstly figured out the effect by the particle approaching the IDEs system with a double-layer effect, and then, explored the dimension and materials for the IDEs system to get a low-cost and relatively high sensitivity of the detection/transducer elements for the sensor design. The central part of the sensor design is the recognition element that employed the DEP force to obtain a label-free capture and separation of cells. The complicated condition of different types of micro-particles in the microfluidic system was investigated thoroughly from a basic model of the plastic bead. Multi-layer models were involved in different types of micro-particles. The real part CM factor, which is the most important impact factor of DEP force, was adjusted by changing the conductivity of the medium solution regarding the reasonable simulation results. The best selection of the conductivity of medium solution is 4000 μS/cm, which can provide a clear separation and capture frequency for HEK_293 cells from other micro-particles such as a plastic bead, Yeast cell, and CHO_7 cell. The frequency and applied voltage were selected at 5MHz and 1V peak to peak when given a flow rate at 120 μm/s. By analyzing the kinetic system of a plastic bead in the micro-channel, an adept way for the capture and separate process in a lower conductivity medium solution was figured out. The simulations on the plastic bead and the size of the particle have a significant effect, and in the thesis condition, it provided a positive effect during the capture process. And finally, the HEK_293 can get captured and separated in a lower medium solution at 200 μS/cm and 1500 μS/cm. This can be helpful to keep cells live in the microfluidic system. In the POC or LOC purpose, like drug detection, a longer experiential period will be required.

5.2. Ongoing work

This thesis was based on the theory and simulation to guide the IDEs system and microfluidic design. It figures out the direction and can avoid unnecessary issues with experiments. For the future work, the IDEs system could be improved with a physical restriction such as a micro-well to capture the single cell, which is more accurate and practical to be utilized in the industrial application. Also, in the thesis, four different types of models of the micro-particle were simulated and explored. These four models selected were representatives for all common particles in the medicine, agriculture, and other industrial environments. For a specific condition such as a blood sample with the cancer cell, to detect the cancer cell which could easily to set up a new model based on this thesis work and design the custom chips for specific applications. Therefore, wider area groups of sample combinations could be explored in further work.

Reference

[1] Lindholm-Sethson, B.; Nyström, J.; Geladi, P.; Koeppe, R.; Nelson, A.; Whitehouse, C. Are biosensor arrays in one membrane possible? A combination of multifrequency impedance measurements and chemometrics. Anal. Bioanal. Chem. 2003, 377, 478–485.

[2] Sackmann EK, Fulton AL, Beebe DJ. "The present and future role of microfluidics in biomedical research", Nature. 507:181–189. [PubMed: 24622198], 2014.

[3] Clin. Chim. Acta, "Does POCT reduce the risk of error in laboratory testing", vol. 404, no. 1, pp. 59–64, 2009.

[4] Vashist SK, Luppa PB, Yeo LY, Ozcan A, Luong JH. "Emerging Technologies for Next-Generation Point-of-Care Testing." Trends in biotechnology. 33:692–705. [PubMed: 26463722], 2015.

[5] Hitzbleck M, Delamarche E. "Optical sensor arrays for chemical sensing: the optoelectronic nose" Chem Soc Rev. 42:8494–8516. [PubMed: 23925517], 2013.

[6] Sharma S, Zapatero-Rodriguez J, Estrela P, O'Kennedy R. Biosensors. "Point-of-Care Diagnostics in Low Resource Settings: Present Status and Future Role of Microfluidics" 5:577–601. [PubMed: 26287254], 2015.

[7] Li Y, Xuan J, Song Y, Qi W, He B, Wang P, Qin L. ACS Nano. "Nanoporous Glass Integrated in Volumetric Bar-Chart Chip for Point-of-Care Diagnostics of Non-Small Cell Lung Cancer" 10:1640–1647. [PubMed:26690745], 2016.

[8] Mohanty, S.P.; Kougianos, E. Biosensors: A tutorial review. IEEE Potentials 2006, 25, 35–40.

[9] Subrahmanyam, S.; Piletsky, S.A.; Turner, A.P.F. Application of Natural Receptors in Sensors and Assays. Anal. Chem. 2002, 74, 3942–3951.

[10] Lindholm-Sethson, B.; Nyström, J.; Geladi, P.; Koeppe, R.; Nelson, A.; Whitehouse, C. Are biosensor arrays in one membrane possible? A combination of multifrequency impedance measurements and chemometrics. Anal. Bioanal. Chem. 2003, 377, 478–485.

[11] J.P.Chambers, B.P.Arulanandam 2008, "Biosensor Recognition Elements", DEFENSE TECHNICAL INFORMATION CENTER, 14, ADA541989.

[12] V. K. Omachonu, "Innovation in Healthcare Delivery Systems : A Conceptual Framework," Innov. J., vol. 15, no. 1, pp. 1–20, 2010.

[13] G. Luka"Microfluidics integrated biosensors: A leading technology towards

lab-on- A-chip and sensing applications," Sensors (Switzerland), vol. 15, no. 12, pp. 30011–30031, 2015.

[14] N.Bhalla, P.Jolly "Introduction to Biosensors", Biochemistry, 60 1-8, DOI:10.1042/EBC20150001, 2016.

[15] Rasooly, A.; Jacobson, J. Development of biosensors for cancer clinical testing. Biosens. Bioelectron. 2006, 21, 1851–1858.

[16] Wang, J.; Ren, L.; Li, L.; Liu, W.; Zhou, J.; Yu, W.; Tong, D.; Chen, S. Microfluidics: A new cosset for neurobiology. Lab Chip 2009, 9, 644–652.

[17] Danielsa, J.S. Label-Free Impedance Biosensors: Opportunities and Challenges. Electroanalysis 2008, 19, 1239–1257.

[18] Guo, X.; Kulkarni, A.; Doepke, A.; Halsall, H.B.; Iyer, S.; Heineman, W.R. Carbohydrate-Based Label-Free Detection of Escherichia coli ORN 178 Using Electrochemical Impedance Spectroscopy. Anal. Chem. 2012, 84, 241–246.

[19] Shi, W.; Ma, Z. A novel label-free amperometric immunosensor for carcinoembryonic antigen based on redox membrane. Biosens. Bioelectron. 2011, 26, 3068–3071.

[20] Qiu, J.D.; Huang, H.; Liang, R.P. Biocompatible and label-free amperometric immunosensor for hepatitis B surface antigen using a sensing film composed of poly(allylamine)-branched ferrocene and gold nanoparticles. Microchim. Acta 2011, 174, 97–105.

[21] Zelada-Guillén, G.A.; Tweed-Kent, A.; Niemann, M.; Göringer, H.U.; Riu, J.; Rius, F.X. Ultrasensitive and real-time detection of proteins in blood using a potentiometric carbon-nanotube aptasensor. Biosens. Bioelectron. 2013, 41, 366–371.

[22] Koncki, R. Recent developments in potentiometric biosensors for biomedical analysis. Anal. Chim. Acta 2007, 599, 7–15.

[23] Guo, X. Surface plasmon resonance based biosensor technique: A review. J. Biophotonics 2012, 5, 483–501.

[24] Tawil, N.; Sacher, E.; Mandeville, R.; Meunier, M. Surface plasmon resonance detection of E. coli and methicillin-resistant S. aureus using bacteriophages. Biosens. Bioelectron. 2012, 37, 24–29.

[25] Tamayo, J.; Kosaka, P.M.; Ruz, J.J.; San Paulo, Á.; Calleja, M. Biosensors based on nanomechanical systems. Chem. Soc. Rev. 2013, 42, 1287–1311.

[26] Liu, Y.; Schweizer, L.M.; Wang, W.; Reuben, R.L.; Schweizer, M.; Shu, W. Label-free and real-time monitoring of Yeast cell growth by the bending of

polymer microcantilever biosensors. Sens. Actuators B Chem. 2013, 178, 621–626.

[27] Lu, C.H.; Zhang, Y.; Tang, S.F.; Fang, Z.B.; Yang, H.H.; Chen, X.; Chen, G.N. Sensing HIV related protein using epitope imprinted hydrophilic polymer coated quartz crystal microbalance. Biosens. Bioelectron. 2012, 31, 439–444.

[28] Cheng, C.I.; Chang, Y.-P.; Chu, Y.-H. Biomolecular interactions and tools for their recognition: Focus on the quartz crystal microbalance and its diverse surface chemistries and applications. Chem. Soc. Rev. 2012, 41, 1947–1971.

[29] N.Mazlan, M.Ramli, "Interdigitated electrodes as impedance and capacitance biosensors: A review", AIP Conference proceedings, 020276: https://doi.org/10.1063/1.5002470, 2017.

[30] V.thivina, U.Hashim "Design and fabrication of Interdigitated Electrode (IDE) for detection of Ganoderma boninense", ICSE, DOI:10.1109/SMELEC.2016.7573588, Aug. 2016.

[31] J. Wang, "Glucose biosensors: 40 years of advances and challenges," Electroanalysis, vol. 13, no. 12, pp. 983–988, 2001.

[32] X. Zeng, Z. Shen, and R. Mernaugh, "Recombinant antibodies and their use in

[33] biosensors.," Anal. Bioanal. Chem., vol. 402, no. 10, pp. 3027–38, Apr. 2012.

[34] Z.Zou, "A Polymer Microfluidic Chip With Interdigitated Electrodes Arrays for Simultaneous Dielectrophoretic Manipulation and Impedimetric Detection of Microparticles" IEEE SENSORS VOL.8 NO.5, DOI: 10.1109/JSEN.2008.918907 May, 2008.

[35] J. A. Capobianco, W. Y. Shih, Q. A. Yuan, G. P. Adams, and W. H. Shih, "Label-free, allelectrical, in situ human epidermal growth receptor 2 detection," Rev. Sci. Instrum., vol. 79, no. 7, pp. 3–5, 2008

[36] T.B. Jones, "Basic Theory of Dielectrophoresis and Electrorotation", CIRCUIT, Corbis. Corp. P33-p43, 1998.

[37] D.Showers, S.Qian "Microfluidic separation of live and dead yeast cells using reservoir-based dielectrophoresis" Biomicrofluidics, 6(3): 34102, DOI: 10.1063/1.4732800. Sep.2012.

[38] M. Varshney and Y. Li, "Interdigitated array microelectrode based impedance biosensor coupled with magnetic nanoparticle-antibody conjugates for detection of Escherichia coli O157:H7 in food samples.," Biosens. Bioelectron., vol. 22, no. 11, pp. 2408–14, May 2007.

[39] D. L. Chapman et al., "A CMOS Electrochemical Impedance Spectroscopy (EIS)

Biosensor Array.," Sensors Actuators, B Chem., vol. 4, no. 1, pp. 379–90, Dec. 2010.

[40] J. Ahn et al., "Electrical immunosensor based on a submicron-gap interdigitated electrode and gold enhancement.," Biosens. Bioelectron., vol. 26, no. 12, pp. 4690–6, Aug. 2011.

[41] R. Ehret, W. Baumann, M. Brischwein, a Schwinde, K. Stegbauer, and B. Wolf, "Monitoring of cellular behaviour by impedance measurements on interdigitated electrode structures.," Biosens. Bioelectron., vol. 12, no. 1, pp. 29–41, Jan. 1997.

[42] E. Valera and A. Rodríguez, "Immunosensors Based on Interdigitated Electrodes for the Detection and Quantification of Pesticides in Food," Mohammed Naguib Abd El-Ghany…, 2011.

[43] A. Bonanni, I. Fernández-Cuesta, X. Borrisé, F. Pérez-Murano, S. Alegret, and M. Valle, "DNA hybridization detection by electrochemical impedance spectroscopy using interdigitated gold nanoelectrodes," Microchim. Acta, vol. 170, pp. 275–281, Apr. 2010.

[44] Y. Iwasaki and M. Morita, "Electrochemical measurements with interdigitated array 131 microelectrodes," Curr. Sep., vol. 1, no. 13, pp. 2–8, 1995.

[45] M. Varshney, Y. Li, B. Srinivasan, and S. Tung, "A label-free, microfluidics and interdigitated array microelectrode-based impedance biosensor in combination with nanoparticles immunoseparation for detection of Escherichia coli O157:H7 in food samples," Sensors Actuators B Chem., vol. 128, no. 1, pp. 99–107, Dec. 2007.

[46] A. Cohen and R. Kunz, "Large-area interdigitated array microelectrodes for electrochemical sensing," Sensors Actuators B Chem., pp. 23–29, 2000.

[47] P. Van Gerwen et al., "Nanoscaled interdigitated electrode arrays for biochemical sensors," Sensors Actuators B Chem., vol. 49, no. 1–2, pp. 73–80, Jun. 1998.

[48] J.Martinez, A.Montalibet. "Effect of electrode material on the sensitivity of interdigitated electrodes used for Electrical Cell-Substrate Impedance Sensing technology". DOI: 10.1109/EMBC.2017.8036948 Conference: 39th Annual International Conference of the IEEE Engineering in Medicine and Biology Society (EMBC), July 2017.

[49] S. M. Radke and E. C. Alocilja, "Design and fabrication of a microimpedance biosensor for bacterial detection," IEEE Sens. J., vol. 4, no. 4, pp. 434–440, 2004.

[50] Lyklema.J and de.Keizer "Electric double-layers Fundamentals of Interface and Colloid Science" vol 2 (New York: Academic) pp 1–232, 1995.

[51] Bockris.O and Reddy.N “Modern Electrochemistry: An Introduction to an Interdisciplinary Area” (Berlin:Springer), 1973.

[52] Schwan.P “Linear and nonlinear electrode polarization and biological materials Ann. Biomed”. Eng. 20 269–88, 1992.

[53] Schwan.P “Determination of biological impedances Physical Techniques in Biological Research” vol 6 (New York: Academic) pp 323–407, 1963.

[54] Davey.L, Markx.H and Kell.B “Substitution and spreadsheet methods for analysing dielectric spectra of biological systems” Eur. Biophys. J. 18 255–65, 1990.

[55] Davey.L and Kell.B “The influence of electrode polarisation on dielectric spectra, with special reference to capacitive biomass measurements. I. Quantifying the effects on electrode polarisation of factors likely to occur during fermentations Bioelectrochem.” Bioenerg. 46 91–103, 1998.

[56] P.Ben “Electrode polarization in dielectric measurements: a review” Measurement Science and Technology. 24 102001, 2013.

[57] Debye.P and Huckel.E Zur Theorie der Elektrolyte. I. ¨ Gefrierpunktserniedrigung und verwandte Erscheinungen (The theory of electrolytes: I. Lowering of freezing point and related phenomena) Phys. Z. 24 185–206, 1923.

[58] H. Helmholtz, “Studien Uber electrische Grenzschichten,” Ann. Phys., vol. 243, no. 7, pp. 337–382, 1879.

[59] M. Gouy, “Sur la constitution de la charge électrique à la surface d’un électrolyte,” J. Phys. Théorique Appliquée, vol. 9, no. 1, pp. 457–468, 1910.

[60] D. L. Chapman, “LI. A contribution to the theory of electrocapillarity,” Philos. Mag. Ser.6, vol. 25, no. 148, pp. 475–481, 1913.

[61] O. Stern, “Zur Theorie Der Elektrolytischen Doppelschicht,” Zeitschrift für Elektrochemie und Angew. Phys. Chemie, vol. 30, no. 21–22, pp. 508–516, 1924.

[62] G.Abdelrasoul, S.MacKay, “Non-Invasive Point-of-Care Device to Diagnose Acute Mesenteric Ischemia” ACS Sens DOI: 10.1021/acssensors.8b00558. Oct, 2018.

[63] S. Guo and S. Dong, “Biomolecule-nanoparticle hybrids for electrochemical biosensors,” Trends Anal. Chem., vol. 28, no. 1, pp. 96–109, 2009.

[64] N. Bhatt, P.-J. J. Huang, N. Dave, and J. Liu, “Dissociation and degradation of thiolmodified DNA on gold nanoparticles in aqueous and organic solvents.,” Langmuir, vol. 27, no. 10, pp. 6132–7, May 2011.

[65] J. M. Pingarrón, P. Yáñez-Sedeño, and A. González-Cortés, “Gold nanoparticle-based electrochemical biosensors,” Electrochim. Acta, vol. 53, no. 19, pp. 5848–5866, 2008.

[66] Scott.MacKay 2017, “Design of an Impedance-based, Gold Nanoparticle Enhanced Biosensor System”, Doctor of Philosophy in Biomedical Engineering, University of Alberta, Edmonton, Canada.

[67] C.Qian, H.Huang “Dielectrophoresis for Bioparticle Manipulation”, International Journal of Molecular Sciences, ISSN: 1422-0067, June 2014.

[68] Pandian babu, Vandana devi, "PROBLEMS IN THE STUDY AND USE OF AC DIELECTROPHORESIS AND THEIR CONSEQUENCES: A STUDY BASED ON COMSOL MULTIPHYSICS MODELING" (2013). All Theses. 1731. https://tigerprints.clemson.edu/all_theses/1731

[69] Jones, T.B. “Electromechanics of particles.” Cambridge University Press. Dec. 1995. ISBN: 9780511574498.

[70] P.Ronald, “Dielectrophoresis: theory, methodology, and biological applications” ISBN-13: 978-1118671450, 2017.

[71] Ramos, A., Morgan, H., Green, N.G. and Castellanos, A., Ac electrokinetics: a review of forces in microelectrode structures, J. Phys. D: Appl. Phys. 1998. 31: p. 2338–2353.

[72] Morgan, H., Green, N.G., Dielectrophoretic investigations of sub-micrometre latex spheres, J. Phys. D: Appl. Phys. 1997. 30: p. 2626–2633.

[73] Arnold, W. M. and Zimmermann, U., Electro-rotation development of a technique for dielectric measurements on individual cells and particles. J. Electrostat. 1998. 21:p. 151–191.

[74] Schnelle, Th., Müller, T., Fiedler, S. and Fuhr, G. The influence of higher moments on particle behaviour in dielectrophoretic field cages. J. Electrostat. 1999. 46: p. 13–28.

[75] Irimajiri, A., T. Hanai, and A. Inouye. 1979. A dielectric theory of ‘‘multi-stratified shell’’ model with its application to a lymphoma cell. J. Theor. Biol. 78:251–269.

[76] V.Raicu, G.Raicu “Dielectric Properties of Yeast Cells as simulated by the two-shell model”, Biochimica et Biophysica Acta 1274 143-148, Feb.1996.

[77] E.Salimi, D.Thomson, “Dielectric model for Chinese hamster ovary cells obtained by dielectrophoresis cytometry”, Biomicrofluidics, Jan.2016.

[78] M. E. Fisher and Y. Levin, “Criticality in ionic fluids: Debye-Huckel theory,

Bjerrum, and beyond," Phys. Rev. Lett., vol. 71, no. 23, pp. 3826–3829, 1993.

[79] A.El-Gaddar, M.Robin, "Assessment of 0.5 T Static Field Exposure Effect on Yeast and HEK Cells Using Electrorotation" Biophysical Journal Vol.104, April. 2013.

[80] R.Soffe, S. Tang. "Discontinuous Dielectrophoresis: A Technique for Investigating the Response of Loosely Adherent Cells to High Shear Stress" BIOSTEC, 2016.

[81] Z.Jouyban, "The Effects of Salt stress on plant growth", TJEAS journal ISSN:2051-0853 July, 2012.